

Radboud Universiteit



MASTER THESIS

**Skyrmion Manipulation in Ultrathin
Films by Modification of Exchange
Interactions**

Matteo Stifano

supervised by
Dr. J.H. MENTINK
Dr. A. PRINCIPI

May 2017

Acknowledgements

This thesis represents the conclusion of my journey as physics student at the Radboud University. A journey marked by beautiful and challenging experiences, where my personal growth on the purely academic side was complementary to a wider cultural and social enrichment in a stimulating international environment.

This last year, spent at the Theory of Condensed Matter group, has given me the opportunity to fully taste the world of scientific research and work in contact with friendly and motivated people. In particular, I consider myself privileged to have been supervised by Johan and Alessandro, whose inputs and help constitute the foundation on which this work has been built. I am particularly thankful to them for making me feel one of their colleagues more than just a student.

At last but not least, I want to thank all my friends I shared this journey with and my family, whose support has made all this possible.

Preface

Studies of properties and behaviours of magnetic materials gained the attention both of the academic world and of the general public due to their applicability for information storage devices. Nevertheless, since the first commercial calculator was realized in 1949 [1], the physical concept behind the data reading/writing technology has hardly changed: magnetic domains are ‘written’ on a ferromagnetic film by an electromagnet and the domain polarization inversion is then ‘read’. The domains are typically sub-micrometer sized and the speed with which their polarity can be inverted is limited by the power of the electromagnet used. One of the potential candidates to replace conventional magnetic bits and improve the performances of storage devices are magnetic skyrmions. Indeed, studies on skyrmion-based memories already show promising results that could lead to the development of an ultra-dense, low-cost and low-power storage technology [2–4]. Investigations about skyrmion stability have been widely performed for several lattice structures, both with analytic and numeric tools [5–8], and experimental observations confirm the theoretical predictions [9, 10]. Moreover, it has been shown that it is possible to switch from a skyrmion to a ferromagnetic state and vice versa with electromagnetic fields and spin-polarized currents [6, 11–13]. To further reduce the energy consumption, it may be advantageous to explore new ways to control skyrmions, for example by directly manipulating the microscopic interactions that are responsible for their existence.

The main results shown in this thesis focus on a numerical analysis performed by considering a two-dimensional square lattice of atomic spins. This is considered as a minimal model for a magnetic ultrathin film in which the existence of a skyrmion structure is due to microscopic interactions emerging from heavy-metal substrates on which the magnetic film is grown. The simplified model we study allows for direct comparison with existing analytical/numerical studies for continuous systems [5] and to compute the phase diagram of different spin textures. The information obtained is used, as a second step, to manipulate skyrmion structures by modifying the antisymmetric exchange interaction in the lattice. This fact allows to introduce a new possible way to switch from a skyrmion to a ferromagnetic state by, for instance, an optical control of such interaction [14]. Moreover, with the same mechanism, we show how it is possible to dynamically change the skyrmion chirality.

In the first chapter, we introduce the model and microscopic interactions that define the energy of the system and the equation of motion that governs its dynamics, together with the way such equation is numerically integrated in the simulations. The second chapter shows static and dynamic studies to benchmark our implementation of the UppASD software package in regimes where a relevant analytical solution is feasible. The third chapter gives an analysis about the stability of the cycloid and skyrmion structure in our system as function of the values of the interaction parameters considered. The fourth chapter shows how a modification of the antisymmetric exchange interaction can induce skyrmion annihilation and chirality inversion.

Contents

1	Introduction	8
1.1	Spin Hamiltonian	8
1.1.1	Exchange interaction	8
1.1.2	Uniaxial anisotropy	12
1.1.3	Antisymmetric exchange interaction	12
1.1.4	Other interaction terms	13
1.2	Micromagnetic model	13
1.2.1	Micromagnetic exchange interaction	14
1.2.2	Micromagnetic uniaxial anisotropy	15
1.2.3	Micromagnetic antisymmetric exchange interaction	16
1.3	Atomistic spin dynamics	16
1.3.1	LLG equation	17
1.3.2	Numerical time integration	18
1.4	Introduction summary	20
2	UppASD benchmark	21
2.1	Static testing	21
2.2	Dynamics testing	24
3	Phase diagram	27
3.1	Cycloid phase diagram	27
3.2	Skyrmion phase diagram	30
4	Switching between magnetic structures	34
4.1	Skyrmion to FM state switching	34
4.2	Skyrmion chirality switching	37
5	Concluding remarks	40
	Appendices	42
A	UppASD input files and codes	42
B	Dynamics testing	43
B.1	Discrete Fourier transform	43
B.2	Error analysis	44
C	Cycloid phase diagram	45
D	Topological charge	45
	References	48

1 Introduction

This chapter introduces the fundamental concepts required to understand the results obtained in this thesis. In the first section, we introduce the Hamiltonian that defines the energy of the atomic spin system, giving to each term a short description about the physical reasons for its existence. In the second section, we discuss a continuum-model approximation for such Hamiltonian. We will derive energy functionals to be used, in the second chapter, for comparison of numerical calculations in the atomic system. In the third section, we discuss the time evolution of our system and how such evolution is numerically implemented. This is of key importance as the main results of this work are obtained by studying the dynamics of the system in different conditions. In the last section, we give an overview of the results obtained in the first two sections, so that to have a quick reference during the reading of the following chapters.

1.1 Spin Hamiltonian

In this section, we discuss the different types of interactions that are relevant for magnetic order and formation of spin textures in ferromagnetic thin films. First, we introduce the exchange interaction, the strongest interaction and responsible for the existence of magnetic order. Second, we discuss weaker interactions such as uniaxial anisotropy and antisymmetric exchange interaction, which stabilize atomic spins along a preferred direction and give rise to non-uniform spin textures, such as cycloids and skyrmions. Finally, we discuss magneto-static interactions.

1.1.1 Exchange interaction

The exchange is usually the strongest magnetic interaction in a solid and it is due to the fundamental quantum properties of the particles involved, together with the electrostatic interaction among them. Its origin can be described with a simple two-electron model, which can be generalized for a more complex system [15–17].

We start by considering two non-interacting electrons, with energy defined by Hamiltonians $\hat{\mathcal{H}}_1$ and $\hat{\mathcal{H}}_2$ and eigenfunctions $\psi_a(\mathbf{r}_1)$ and $\psi_b(\mathbf{r}_2)$ respectively, a and b specifying the quantum states and \mathbf{r}_1 and \mathbf{r}_2 the positions. Assuming that the spin of each particle does not affect its motion (thus, for instance, no spin-orbit-interaction term or external magnetic field gradient involved), we can write each electron wave function as product of a spatial term and a spin term, as follows

$$\begin{aligned}\psi_a(\mathbf{r}_1) &= \phi_a(\mathbf{r}_1)\chi_1, \\ \psi_b(\mathbf{r}_2) &= \phi_b(\mathbf{r}_2)\chi_2,\end{aligned}\tag{1}$$

with χ_i ($i = 1, 2$), eigenstates of the spin operator \hat{S}_{iz} ¹, assuming two

¹In principle, we could have considered the eigenstates of the operator \hat{S}_{ix} or \hat{S}_{iy} as well.

distinct values denoted by $|+\rangle$ and $|-\rangle$, where

$$\hat{S}_{iz} |\pm\rangle = \pm \frac{\hbar}{2} |\pm\rangle. \quad (2)$$

Our aim is now to construct a wave function that describes an interacting two-electrons system. The new Hamiltonian is represented by the sum of the single-electron Hamiltonians plus an interaction term, which corresponds to the Coulomb interaction between the two electrons. Thus, we can write

$$\hat{\mathcal{H}} = \hat{\mathcal{H}}^{(0)} + \hat{\mathcal{H}}_{int} = \hat{\mathcal{H}}_1 + \hat{\mathcal{H}}_2 + \hat{\mathcal{H}}_{int}, \quad (3)$$

with

$$\hat{\mathcal{H}}_{int} = \frac{e^2}{|\mathbf{r}_1 - \mathbf{r}_2|}, \quad (4)$$

where e represents the elementary charge. Assuming that the interaction energy is small compared with the total energy, we can determine the wave function of the system with a perturbation theory approach. Thus, we use the eigenfunction of $\hat{\mathcal{H}}^{(0)}$, linear combination of $\psi_a(\mathbf{r})$ and $\psi_b(\mathbf{r})$, as an approximated one for $\hat{\mathcal{H}}$. Since spin does not affect the orbital motion, we can write the total wave function as product of a spatial term and a spin term, as previously. Taking into account the Pauli exclusion principle, we construct the antisymmetric and the symmetric² spin terms and we couple them with the symmetric and antisymmetric spatial terms, respectively, to obtain an antisymmetric total wave function. In order to construct the spin terms, we first find common eigenstates of the spin operators \hat{S}^2 and \hat{S}_z , where

$$\begin{aligned} \hat{S}^2 &= \hat{S}_1^2 + \hat{S}_2^2 + 2\hat{\mathbf{S}}_1 \cdot \hat{\mathbf{S}}_2, \\ \hat{S}_z &= \hat{S}_{1z} + \hat{S}_{2z}. \end{aligned} \quad (5)$$

We thus obtain an antisymmetric singlet state (χ_s) and a symmetric triplet state (χ_t) [18]. By constructing antisymmetric total wave functions of the two-electrons system, we obtain

$$\begin{aligned} \Psi_s(\mathbf{r}_1, \mathbf{r}_2) &= \frac{1}{\sqrt{2}} [\phi_a(\mathbf{r}_1)\phi_b(\mathbf{r}_2) + \phi_a(\mathbf{r}_2)\phi_b(\mathbf{r}_1)]\chi_s, \\ \Psi_t(\mathbf{r}_1, \mathbf{r}_2) &= \frac{1}{\sqrt{2}} [\phi_a(\mathbf{r}_1)\phi_b(\mathbf{r}_2) - \phi_a(\mathbf{r}_2)\phi_b(\mathbf{r}_1)]\chi_t. \end{aligned} \quad (6)$$

As a next step, we compute the energy difference between these two states. Starting with the Hamiltonian of the system, as defined in Eq. (3), the singlet

This choice affects the structure of the eigenstates but not their eigenvalues. Note that the subscript i is just a label to distinguish the two electrons.

²Symmetry relative to exchange of the two particles.

and triplet energies are expressed as follows³

$$\begin{aligned} E_s &= \langle \Psi_s | \hat{\mathcal{H}} | \Psi_s \rangle \equiv \int \Psi_s^* \hat{\mathcal{H}} \Psi_s d\mathbf{r}_1 d\mathbf{r}_2, \\ E_t &= \langle \Psi_t | \hat{\mathcal{H}} | \Psi_t \rangle \equiv \int \Psi_t^* \hat{\mathcal{H}} \Psi_t d\mathbf{r}_1 d\mathbf{r}_2. \end{aligned} \quad (7)$$

By substituting Eq. (6) into Eq. (7) and taking into account the orthonormality of the spatial terms $\phi_a(\mathbf{r})$ and $\phi_b(\mathbf{r})$, one finds

$$E_s - E_t = \int (\Psi_s^* \hat{\mathcal{H}}_{int} \Psi_s - \Psi_t^* \hat{\mathcal{H}}_{int} \Psi_t) d\mathbf{r}_1 d\mathbf{r}_2, \quad (8)$$

which, taking into account the orthonormality of the spin terms χ_s and χ_t , can be rewritten as

$$E_s - E_t = 2 \int \phi_a^*(\mathbf{r}_1) \phi_b^*(\mathbf{r}_2) \hat{\mathcal{H}}_{int} \phi_a(\mathbf{r}_2) \phi_b(\mathbf{r}_1) d\mathbf{r}_1 d\mathbf{r}_2. \quad (9)$$

Knowing the electron spin quantum number and considering Eq. (5), we easily find that⁴

$$\begin{aligned} \langle \mathbf{S}_1 \cdot \mathbf{S}_2 \rangle_s &= -\frac{3}{4} \hbar^2, \\ \langle \mathbf{S}_1 \cdot \mathbf{S}_2 \rangle_t &= \frac{1}{4} \hbar^2. \end{aligned} \quad (10)$$

We can therefore write, completely generally,

$$\hat{\mathcal{H}}_{int} = \frac{1}{4} (E_s + 3E_t) - \frac{E_s - E_t}{\hbar^2} \mathbf{S}_1 \cdot \mathbf{S}_2. \quad (11)$$

By introducing the *exchange integral* J , defined as

$$J = \frac{E_s - E_t}{\hbar^2} = \frac{2}{\hbar^2} \int \psi_a^*(\mathbf{r}_1) \psi_b^*(\mathbf{r}_2) \hat{\mathcal{H}} \psi_a(\mathbf{r}_2) \psi_b(\mathbf{r}_1) d\mathbf{r}_1 d\mathbf{r}_2, \quad (12)$$

and neglecting the constant term in Eq. (11), we get

$$\hat{\mathcal{H}}_{int} = -J \mathbf{S}_1 \cdot \mathbf{S}_2. \quad (13)$$

Note that, for positive values of J , the triplet state is favoured.

The result obtained so far serves us to understand the physical reasons behind the exchange interaction. Indeed, we have seen how this is nothing but the consequence of the Coulomb interaction and the Pauli exclusion principle.

A formal generalization of Eq. (13) for more electrons is not discussed in details here. Nevertheless, in the following chapters we will make use of a Hamiltonian

³ $\Psi \equiv \Psi(\mathbf{r}_1, \mathbf{r}_2).$

⁴

$\langle \mathbf{S}_1 \cdot \mathbf{S}_2 \rangle_s \equiv \langle \Psi_s | \mathbf{S}_1 \cdot \mathbf{S}_2 | \Psi_s \rangle,$

$\langle \mathbf{S}_1 \cdot \mathbf{S}_2 \rangle_t \equiv \langle \Psi_t | \mathbf{S}_1 \cdot \mathbf{S}_2 | \Psi_t \rangle.$

that recalls the result obtained for a two-electrons system but finds its applicability in a wide range of cases, such as magnetic insulators [19] and ferromagnetic metals [20]. Such a Hamiltonian is widely known as *Heisenberg model* [16]

$$\hat{\mathcal{H}} = -\frac{1}{2} \sum_{ij} J_{ij} \mathbf{S}_i \cdot \mathbf{S}_j. \quad (14)$$

Here, J_{ij} are exchange integrals between atoms on lattice sites i and j and \mathbf{S}_i is the spin operator of the atom on site i . The factor $1/2$ is introduced to avoid double counting. Eq. (14) has a corresponding classical expression, which for metals is qualitatively derived using the atomic-sphere approximation (ASA) [21]. Indeed, considering ASA, we can decouple the atomic spin operators expectation values, so that

$$\langle \hat{\mathcal{H}} \rangle = -\frac{1}{2} \sum_{ij} J_{ij} \langle \mathbf{S}_i \mathbf{S}_j \rangle \approx -\frac{1}{2} \sum_{ij} J_{ij} \langle \mathbf{S}_i \rangle \cdot \langle \mathbf{S}_j \rangle. \quad (15)$$

The electrons can adapt almost instantaneously (femtosecond regime) to the tilt of the atomic spins (for the magnetic structures we will use, nanosecond regime). Thus, using the so-called adiabatic approximation and taking into account the ASA we can assume that the dynamics of the atomic spins does not affect the value of the exchange integrals, which stay constant in time. We can then write the classical Heisenberg model

$$\mathcal{H}_{ex} = -\frac{1}{2} \sum_{ij} J_{ij} \mathbf{m}_i \cdot \mathbf{m}_j, \quad (16)$$

where \mathbf{m}_i is the classical spin of the atom (in general, total angular momentum) on site i . Typically, J_{ij} is short-ranged and by considering nearest neighbors only will, together with the interactions described in the following sections, be sufficient to stabilize the magnetic structures we are interested to investigate. Therefore, we can finally write

$$\mathcal{H}_{ex} = -\frac{J}{2} \sum_{\langle ij \rangle} \mathbf{m}_i \cdot \mathbf{m}_j, \quad (17)$$

where $\langle ij \rangle$ restricts the sum over neighbouring atoms. Without loss of generality, we consider \mathbf{m}_i to represent the atomic magnetic moment⁵, whose magnitude is equal to one μ_B (Bohr magneton). Nevertheless, in the following chapters we still refer to \mathbf{m}_i as atomic spin. From this, it follows that J has dimensions of *energy*/ μ_B^2 .

As can be seen from Eq. (17), positive values of J favor a ferromagnetic behavior, while negative values an antiferromagnetic. In this thesis we focus solely on ferromagnetic systems.

⁵Atomic angular momentum and atomic magnetic moment differ from a multiplication factor only. This is the reason why we can conveniently consider either of them, with a correct rescaling of J .

1.1.2 Uniaxial anisotropy

As we can see from Eq. (17), the exchange interaction is isotropic. Thus, the total magnetization can point in any direction without affecting the energy of the system. However, magnetic materials have in general a preferential direction in space. This is mainly due to spin-orbit coupling [22,23]. In order to take into account this behaviour, an extra term is included in the classical Hamiltonian, the anisotropy energy term ⁶:

$$\mathcal{H}_{an} = \frac{K}{2} \sum_i (\mu_B \sin \theta_i)^2, \quad (18)$$

where θ_i is the angle between the atomic spin vector relative to site i and the easy-axis direction, while $K > 0$ is the *anisotropy constant*, which defines the anisotropy energy. Opposed to exchange, anisotropy is of relativistic origin [24] and, therefore, much smaller than the exchange interaction ($K \sim 0.01 - 0.1J$). Without loss of generality, in what follows we consider the easy-axis directed along the z -axis. Thus, we have ⁷

$$\mathcal{H}_{an} = \frac{NK}{2} - \frac{K}{2} \sum_i (\mathbf{m}_i \cdot \mathbf{e}_z)^2, \quad (19)$$

where \mathbf{e}_z is the z -axis versor and N is the total number of atoms in the sample.

1.1.3 Antisymmetric exchange interaction

The antisymmetric exchange interaction, also called Dzyaloshinskii-Moriya interaction (DMI), was originally predicted for bulk systems with broken inversion symmetry [25,26]. This interaction favors atomic spins to tilt with respect to each other, allowing homogeneous canting and chiral magnetic textures [27,28]. In this work, we will focus on two-dimensional systems, which represent a simplified model for ultrathin magnetic films ($\sim 1\text{-}40$ nm).

Experimentally, large values of DMI occur at the interface between the magnetic thin film and a heavy metal with a strong spin-orbit coupling [5]. In this situation, the Dzyaloshinskii-Moriya interaction Hamiltonian term can be written as

$$\mathcal{H}_{DM} = \frac{D}{2} \sum_{\langle ij \rangle} (\mathbf{u}_{ij} \times \mathbf{e}_z) \cdot (\mathbf{m}_i \times \mathbf{m}_j), \quad (20)$$

where \mathbf{u}_{ij} is the unit vector oriented from site i to site j and \mathbf{e}_z is the direction normal to the film and oriented from the high spin-orbit layer to the magnetic film [5,29] (see Fig. 1). The factor $1/2$ is introduced to avoid double

⁶The $1/2$ factor is introduced to match the analytical model with the Hamiltonian used in the simulation, as we will see later on.

⁷The constant term is kept to match the analytical model with the simulation, as in the previous case.

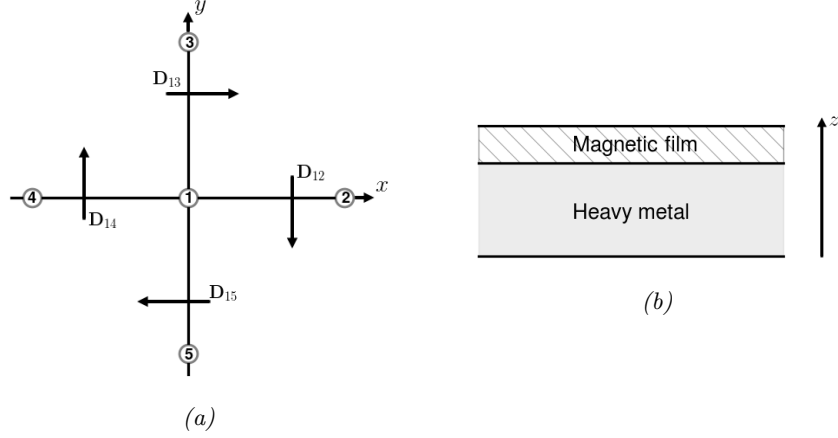


Figure 1: (a) Illustration of the directions of the vectors $\mathbf{D}_{ij} = D \mathbf{u}_{ij} \times \mathbf{e}_z$ in the lattice and (b) schematic illustration of the geometry of the system considered.

counting. Being the DMI due to spin-orbit coupling, we expect D to be much smaller than the exchange constant ($D \sim 0.01 - 0.3J$) [28].

1.1.4 Other interaction terms

So far, three contributions to the spin Hamiltonian have been discussed. Nevertheless, there are additional magnetic interaction terms that might arise in a solid but are not taken into account in our model. Examples of those are the Zeeman and the dipole-dipole interaction terms.

The Zeeman term arises from the interaction between an external applied magnetic field and the atomic spins. This favors the atomic magnetic moments to be aligned along the applied magnetic field direction. We do not discuss it here, since our focus is on dynamics due to changes in exchange interactions.

The dipole-dipole interaction term results from the magnetostatic interaction among atomic spins. Its long-range character determines the magnetic properties of macroscopic systems, but it is negligible for short-range interactions (dipole-dipole interaction energy is approximately 10^{-3} times the exchange interaction energy in the nearest-neighbors range). We neglect this term as we focus on relatively small samples (100 atoms-per-side), where the dipole-dipole interaction does not significantly affect the system total energy.

1.2 Micromagnetic model

In the previous section, we have introduced the spin Hamiltonian, which defines the energy of a system of atomic spins distributed over a discrete lattice. In general, given the high number of atomic spins involved, computing such an energy analytically is not feasible. In this section, we derive a continuum model for our spin Hamiltonian, which will be used, in the next chapter, as a comparison

with the energy of the discrete system numerically evaluated.

The possibility to derive a continuum model is due to the fact that the exchange interaction is the dominant one and, therefore, we expect a slight tilt between neighboring atomic spins and a smooth change of the magnetization direction along the sample. We can then replace the discrete lattice of atomic spins with a continuous varying function $\mathbf{m}(\mathbf{r})$ and the spin Hamiltonian with an energy functional. Hereby, we derive the energy functionals corresponding to the three spin Hamiltonian contributions (exchange, anisotropy and DMI) introduced earlier.

1.2.1 Micromagnetic exchange interaction

Starting from Eq. (17), we now derive the energy functional for the exchange interaction. We consider a two-dimensional square lattice, and, therefore, each atom has four neighbors. In order to go from a discrete model to a continuous one, we need to refer to each atomic site with its Cartesian coordinates. Thus, each atomic site i must be associated to a couple (x_i, y_i) . We can then write

$$\begin{aligned}\mathcal{H}_{ex} &= -\frac{J}{2} \sum_{\langle ij \rangle} \mathbf{m}_i \cdot \mathbf{m}_j \\ &= -\frac{J}{2} \sum_{\langle ij \rangle} \mathbf{m}(x_i, y_i) \cdot \mathbf{m}(x_j, y_j) \\ &= -\frac{J}{2} \sum_i \mathbf{m}(x_i, y_i) [\mathbf{m}(x_i + a, y_i) + \mathbf{m}(x_i - a, y_i) \\ &\quad + \mathbf{m}(x_i, y_i + a) + \mathbf{m}(x_i, y_i - a)],\end{aligned}$$

where a is the lattice constant, *i.e.* the distance between neighboring atoms. In the continuum approximation ($a \ll L$, with L the system size), we can Taylor-expand

$$\begin{aligned}\mathbf{m}(x_i \pm a, y_i) &\simeq \mathbf{m}(x_i, y_i) \pm a \partial_x \mathbf{m}(x_i, y_i) + \frac{a^2}{2} \partial_x^2 \mathbf{m}(x_i, y_i), \\ \mathbf{m}(x_i, y_i \pm a) &\simeq \mathbf{m}(x_i, y_i) \pm a \partial_y \mathbf{m}(x_i, y_i) + \frac{a^2}{2} \partial_y^2 \mathbf{m}(x_i, y_i).\end{aligned}\tag{21}$$

Our exchange interaction Hamiltonian then becomes

$$\mathcal{H}_{ex} \simeq -\frac{J}{2} \sum_i \mathbf{m}(x_i, y_i) [4\mathbf{m}(x_i, y_i) + a^2 \partial_x^2 \mathbf{m}(x_i, y_i) + a^2 \partial_y^2 \mathbf{m}(x_i, y_i)].$$

All atomic spins have magnitude equals to μ_B^2 . Thus, with $\mathbf{m}_i \equiv \mathbf{m}(x_i, y_i)$:

$$\begin{aligned}
\mathbf{m}_i \cdot \mathbf{m}_i &= \mu_B^2 \\
\implies (\partial_{x,y} \mathbf{m}_i) \cdot \mathbf{m}_i + \mathbf{m}_i \cdot (\partial_{x,y} \mathbf{m}_i) &= 0 \\
\implies \mathbf{m}_i \cdot (\partial_{x,y} \mathbf{m}_i) &= 0 \\
\implies (\partial_{x,y} \mathbf{m}_i)^2 &= -\mathbf{m}_i \cdot (\partial_{x,y}^2 \mathbf{m}_i),
\end{aligned}$$

From this follows

$$\begin{aligned}
\mathcal{H}_{ex} &\simeq -\frac{J}{2} \sum_i 4 - a^2 [(\partial_x \mathbf{m}_i)^2 + (\partial_y \mathbf{m}_i)^2] \\
&\simeq -2NJ + \frac{J}{2} \sum_i a^2 [(\nabla m_{ix})^2 + (\nabla m_{iy})^2 + (\nabla m_{iz})^2],
\end{aligned}$$

where N is the number of atoms in our sample. Turning a summation over discrete elements into an integral, we obtain our final functional

$$\mathcal{H}_{ex} \simeq -2NJ + \frac{J}{2} \iint [(\nabla m_x)^2 + (\nabla m_y)^2 + (\nabla m_z)^2] dx dy \equiv \varepsilon_{ex}. \quad (22)$$

The first term represents the minimum energy the system can reach, and corresponds to a configuration where all atomic spins are aligned. The second term represents the increment in exchange interaction energy due to the tilt of atomic spins from the minimum-energy configuration.

1.2.2 Micromagnetic uniaxial anisotropy

Deriving the functional relative to the uniaxial anisotropy energy is more straightforward than the exchange interaction. Starting from Eq. (19) and taking into account all the considerations made in the previous section, we can proceed with the derivation as follows:

$$\begin{aligned}
\mathcal{H}_{an} &= \frac{NK}{2} - \frac{K}{2} \sum_i (\mathbf{m}_i \cdot \mathbf{e}_z)^2 \\
&= \frac{NK}{2} - \frac{K}{2a^2} \sum_i a^2 (\mathbf{m}_i \cdot \mathbf{e}_z)^2.
\end{aligned}$$

In the continuum limit, the final expression becomes

$$\mathcal{H}_{an} \simeq \frac{NK}{2} - \frac{K}{2a^2} \iint m_z^2 dx dy \equiv \varepsilon_{an}. \quad (23)$$

The presence of the first (constant) term, together with the $1/2$ multiplication factor, is only due to the way the anisotropy energy calculation has been implemented in the software package used (see following section) and, thus, to make the continuum model comparable with the numerical results (following chapter).

1.2.3 Micromagnetic antisymmetric exchange interaction

Deriving the functional relative to the DMI follows a procedure similar to what seen for the exchange interaction, replacing spins of neighboring sites with corresponding Taylor-expansions (Eq. (21)). Starting from Eq. (20), we have

$$\begin{aligned}
\mathcal{H}_{DM} &= \frac{D}{2} \sum_{\langle i,j \rangle} (\mathbf{u}_{ij} \times \mathbf{e}_z) \cdot (\mathbf{m}_i \times \mathbf{m}_j) \\
&= \frac{D}{2} \sum_{\langle i,j \rangle} (\mathbf{u}_{ij} \cdot \mathbf{m}_i)(\mathbf{e}_z \cdot \mathbf{m}_j) - (\mathbf{u}_{ij} \cdot \mathbf{m}_j)(\mathbf{e}_z \cdot \mathbf{m}_i), \\
&= \frac{D}{2} \sum_i m_x(x_i, y_i) [m_z(x_i + a, y_i) - m_z(x_i - a, y_i)] \\
&\quad - m_z(x_i, y_i) [m_x(x_i + a, y_i) - m_x(x_i - a, y_i)] \\
&\quad + m_y(x_i, y_i) [m_z(x_i, y_i + a) - m_z(x_i, y_i - a)] \\
&\quad - m_z(x_i, y_i) [m_y(x_i, y_i + a) - m_y(x_i, y_i - a)] \\
&= \frac{D}{a} \sum_i a^2 (m_{ix} \partial_x m_{iz} - m_{iz} \partial_x m_{ix} + m_{iy} \partial_y m_{iz} - m_{iz} \partial_y m_{iy}).
\end{aligned}$$

Note that the second line has been derived using a cross product property⁸ and we have considered $m_{i\alpha} \equiv m_\alpha(x_i, y_i)$, $\alpha = x, y$, in the last line. In the continuum limit, the final expression is

$$\mathcal{H}_{DM} \simeq \frac{D}{a} \iint (m_x \partial_x m_z - m_z \partial_x m_x + m_y \partial_y m_z - m_z \partial_y m_y) dx dy \equiv \varepsilon_{DM}. \quad (24)$$

We have so obtained the result found in [5, 30]. Note that, opposed to exchange, here only first derivatives remain⁹.

1.3 Atomistic spin dynamics

As introduced previously, the aim of this thesis is to investigate the stability of certain magnetic structures in relation with the value of the interaction parameters adopted and in which conditions it is possible to dynamically change the magnetic texture from one stable structure to another one. This is the reason why, in this section, we introduce the equation that defines the dynamics of the atomic spins and we explain how we compute such dynamics.

⁸ $(\mathbf{a} \times \mathbf{b}) \cdot (\mathbf{c} \times \mathbf{d}) = (\mathbf{a} \cdot \mathbf{c})(\mathbf{b} \cdot \mathbf{d}) - (\mathbf{a} \cdot \mathbf{d})(\mathbf{b} \cdot \mathbf{c})$.

⁹The next order term is a third order derivative which we ignore here.

1.3.1 LLG equation

In the following, we introduce the equation of motion that defines the dynamics of each atomic spin in the system.

We start by considering the motion of a single atomic spin \mathbf{m}_i under a magnetic field \mathbf{B}_i . Due to conservation of angular momentum, the variation in time of the atomic spin is defined by the torque \mathbf{T}_i felt for the presence of the magnetic field [31]. Thus

$$\frac{d\mathbf{m}_i}{dt} = \mathbf{T}_i = -\gamma \mathbf{m}_i \times \mathbf{B}_i, \quad (25)$$

where γ is the electron gyromagnetic ratio. Eq. (25) leads the atomic spin to precess around the magnetic field with the Larmor frequency $f_i = \frac{\gamma}{2\pi} |\mathbf{B}_i|$ (see Fig. 2).

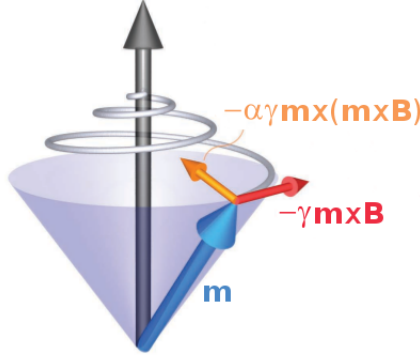


Figure 2: Illustration of the motion of an atomic spin \mathbf{m} under a magnetic field \mathbf{B} , highlighting the purely precessional term (red) and the damping term (orange). Figure adapted from [32].

Note that the previous relation conserves the atomic spin magnitude, but does not explain how the atomic spin can eventually align along the field direction and reach the equilibrium position, behaviour experimentally observed as consequence of interactions with lattice vibrations, conduction electrons or other external sources [33,34]. Landau and Lifshitz [35] proposed to add a term proportional to $\mathbf{m}_i \times (\mathbf{m}_i \times \mathbf{B}_i)$, which conserves the atomic spin magnitude, while Gilbert [36] suggested to add a viscous force proportional to $\mathbf{m}_i \times \frac{d\mathbf{m}_i}{dt}$. With a renormalization term, the two suggestions are equivalent and lead to the well-known Landau-Lifschitz-Gilbert (LLG) equation

$$\frac{d\mathbf{m}_i}{dt} = -\gamma [\mathbf{m}_i \times \mathbf{B}_i] - \frac{\alpha\gamma}{\mu_B} [\mathbf{m}_i \times (\mathbf{m}_i \times \mathbf{B}_i)]. \quad (26)$$

The dimensionless constant $\alpha > 0$ takes the name of damping parameter and represents all relaxation mechanisms. As next step, we want to identify

the effective magnetic field felt by each atomic spin \mathbf{m}_i . Previously, we have introduced the Hamiltonian that defines the energy of the discrete system. We can represent such Hamiltonian in a more general way as sum of energies of atomic spins in some effective fields. We can thus write

$$\mathcal{H} = \mathcal{H}_{ex} + \mathcal{H}_{an} + \mathcal{H}_{DM} = - \sum_i \mathbf{m}_i \cdot \mathbf{B}_i. \quad (27)$$

Therefore, each effective field \mathbf{B}_i is unambiguously defined by \mathcal{H} and by the system configuration, as follows:

$$\mathbf{B}_i = - \frac{\partial \mathcal{H}}{\partial \mathbf{m}_i}. \quad (28)$$

Note that, unless the system is in an equilibrium state, each effective field is time dependent.

For numerical integration, it is convenient to write the LLG equation in dimensionless form. This is achieved by writing $\mathbf{m}_i = \tilde{\mathbf{m}}_i \mu_B$, with $\tilde{\mathbf{m}}_i$ dimensionless unit vector, and expressing the Hamiltonian as $\mathcal{H} = \tilde{\mathcal{H}} \tilde{J} / \mu_B^2$, with $\tilde{\mathcal{H}}$ the dimensionless Hamiltonian and \tilde{J} the exchange interaction in units of energy. Thus

$$\frac{d\tilde{\mathbf{m}}_i}{d\tau} = \left[\tilde{\mathbf{m}}_i \times \frac{\partial \tilde{\mathcal{H}}}{\partial \tilde{\mathbf{m}}_i} \right] + \alpha \left[\tilde{\mathbf{m}}_i \times (\tilde{\mathbf{m}}_i \times \frac{\partial \tilde{\mathcal{H}}}{\partial \tilde{\mathbf{m}}_i}) \right], \quad (29)$$

where $\tau = \gamma \tilde{J} t / \mu_B \simeq 2 \tilde{J} t / \hbar$.

1.3.2 Numerical time integration

As we have seen, the dynamics of our system is completely described by Eq. (26) and by the Hamiltonian $\mathcal{H} = \mathcal{H}_{ex} + \mathcal{H}_{an} + \mathcal{H}_{DM}$, which defines the effective magnetic field for each atomic site for a given system configuration. Indeed, from Eq. (28) we note that the effective field felt by each atomic spin depends on the configuration of all the other atomic spins in the instant considered. Taking into account that, in this work, we will deal with a system of 10^4 atoms, it is clear that the use of a numerical integrator is needed in order to evaluate the dynamics of the system. In the following, we describe how the numerical integration of the LLG equation is performed in the software package used for our simulations, the UppASD (v3.0) [37].

There are several numerical methods with which the LLG equation can be integrated. Each of them differs for accuracy, stability and computational complexity [38]. Here, we focus on the description of the semi-implicit midpoint scheme and, in particular, on the SIB method in [39], scheme adopted for the simulations in this thesis.

Considering the simulation time interval $[0, T]$, we divide such interval into n time steps $\Delta\tau$, so that $T = n\Delta\tau$. Being $\tilde{\mathbf{m}}_i^\tau$ the atomic spin on site i at time τ ,

the aim is to find $\tilde{\mathbf{m}}_i^{\tau+\Delta\tau}$ for $i = 1, \dots, N$, with N number of spins in the system. In order to simplify the notation, we introduce the vector

$$\mathbf{A}_i(\tilde{\mathbf{m}}^\tau) = -\mathbf{B}_i(\tilde{\mathbf{m}}^\tau) - \alpha\tilde{\mathbf{m}}_i \times \mathbf{B}_i(\tilde{\mathbf{m}}^\tau), \quad (30)$$

where $\mathbf{B}_i(\tilde{\mathbf{m}}^\tau)$ stresses the dependence of the effective magnetic field on the configuration of all other spins at time τ . The update rule is the following:

$$\begin{aligned} \tilde{\mathbf{m}}_i^\tau &= \tilde{\mathbf{m}}_i^\tau + \Delta\tau \frac{\tilde{\mathbf{m}}_i^\tau + \tilde{\mathbf{m}}_i^\tau}{2} \times \mathbf{A}_i(\tilde{\mathbf{m}}^\tau) \\ \tilde{\mathbf{m}}_i^{\tau+\Delta\tau} &= \tilde{\mathbf{m}}_i^\tau + \Delta\tau \frac{\tilde{\mathbf{m}}_i^\tau + \tilde{\mathbf{m}}_i^{\tau+\Delta\tau}}{2} \times \mathbf{A}_i\left(\frac{\tilde{\mathbf{m}}^\tau + \tilde{\mathbf{m}}^\tau}{2}\right), \end{aligned} \quad (31)$$

where $\tilde{\mathbf{m}}_i^\tau$ must be evaluated for all $i = 1, \dots, N$ before computing $\tilde{\mathbf{m}}_i^{\tau+\Delta\tau}$. This requires to solve two systems of three coupled equations for each spin, at each time-step. Since this can be done analytically, the semi-implicit scheme is, de facto, explicit. Moreover, it can be formally shown that, in Eq. (31), norm-preservation for each atomic spin is assured and, in the case of a two-spins system with zero damping, both energy and total spin are conserved quantities [39]. Both features relate with the stability of the algorithm: since norm-preservation is an intrinsic property of the update rule (no renormalization step required), the numerical integration stays close to the real dynamics, even with relatively big time-steps [40]; Moreover, the time-dependence of the effective field is the main source of instability and the effective field computation is directly related with the total spin of the system [39].

The computational complexity of the semi-implicit midpoint scheme is comparable with standard explicit integration schemes, such as the Euler [38] or the Heun [41]. However, these schemes do not intrinsically preserve vectors norm nor total spin and, therefore, are not as stable as the semi-implicit scheme [39]. Implicit integration schemes, such as the midpoint scheme [42], have the same built-in conservation features of the SIB but require a much higher computational effort. For instance, in the case of the midpoint scheme, for each time-step, a system of $3N$ coupled equations needs to be solved numerically.

We conclude that the semi-implicit midpoint scheme successfully combines the computational efficiency of explicit schemes with the stability of implicit schemes. All the schemes mentioned are of second order, except for the Euler scheme, which is of first order. Thus, they are all comparable in accuracy.

For the analysis performed in the following chapters, we must take into account that in UppASD each time step is expressed in picoseconds. Nevertheless, all the results in this thesis will be given using the dimensionless quantity τ (see Eq. (29)). As detailed in App. A, typically we use $\tilde{J} = 2.127 \cdot 10^{-3} mRy$ and a time step of $\Delta t_{step} = 1 \text{ ps}$, such that

$$\Delta\tau_{step} \simeq 2\tilde{J}\Delta t_{step}/\hbar = 0.088 \quad (32)$$

represents the time step unit for the dimensionless quantity τ . Below, we consider simulations with different step size in the numerical integration, taking $\Delta\tau_{step}$ as reference. For completeness, we mention that Eq. (31) can be

implemented with stochastic terms so that to simulate a finite-temperature behavior [39]. The detailed description of the algorithm is not relevant for this work as we will perform simulations at zero temperature only.

1.4 Introduction summary

To conclude this chapter, we schematically summarize the results discussed in this introduction concerning the atomistic Hamiltonians and the energy functionals of the continuum model, which will be used in the next chapter to check numerics. It is important to mention that the numerical results showed in this thesis are obtained by studying a two-dimensional square-lattice system where periodic boundary conditions (PBC) are applied.

Exchange	
Discrete	$\mathcal{H}_{ex} = -\frac{J}{2} \sum_{\langle ij \rangle} \mathbf{m}_i \cdot \mathbf{m}_j$
Continuum	$\varepsilon_{ex} = -2NJ + \frac{J}{2} \iint [(\nabla m_x)^2 + (\nabla m_y)^2 + (\nabla m_z)^2] dx dy$
Anisotropy	
Discrete	$\mathcal{H}_{an} = \frac{NK}{2} - \frac{K}{2} \sum_i (\mathbf{m}_i \cdot \mathbf{e}_z)^2$
Continuum	$\varepsilon_{an} = \frac{NK}{2} - \frac{K}{2a^2} \iint m_z^2 dx dy$
DMI	
Discrete	$\mathcal{H}_{DM} = \frac{D}{2} \sum_{\langle ij \rangle} (\mathbf{u}_{ij} \times \mathbf{e}_z) \cdot (\mathbf{m}_i \times \mathbf{m}_j)$
Continuum	$\varepsilon_{DM} = \frac{D}{a} \iint m_x \frac{\partial m_z}{\partial x} - m_z \frac{\partial m_x}{\partial x} + m_y \frac{\partial m_z}{\partial y} - m_z \frac{\partial m_y}{\partial y} dx dy$

Table 1: Table showing the atomistic Hamiltonians and the energy functionals of the continuum model.

2 UppASD benchmark

In this chapter, we will benchmark the UppASD software package by performing a static and a dynamic test, relevant to the static and dynamics properties of the magnetic textures investigated in Ch. 3 and Ch. 4, respectively. The static test involves a comparison between the energy terms of the discrete system numerically computed and the continuum-model functionals, by using a cycloid as magnetic structure. In the dynamic test we investigate the numerical integration of the LLG equation by reproducing the spin wave dispersion relation in a one-dimensional spin chain.

2.1 Static testing

In this section, we examine whether the energy terms of a cycloid structure in the atomistic model converge to their corresponding energy functionals while increasing the number of atoms per cycloid wavelength.

The cycloid, as illustrated in Fig. 3, is one of the magnetic structures stabilized by the DMI [5]. We consider such a structure evolving along the x-axis as given by the following expression¹⁰:

$$\begin{aligned}\tilde{m}^x(x) &= \cos \frac{2\pi}{\lambda} x, \\ \tilde{m}^y(x) &= 0, \\ \tilde{m}^z(x) &= \sin \frac{2\pi}{\lambda} x,\end{aligned}\tag{33}$$

where $\tilde{\mathbf{m}}(x) = \mathbf{m}(x)/\mu_B$ and λ defines the cycloid wavelength.

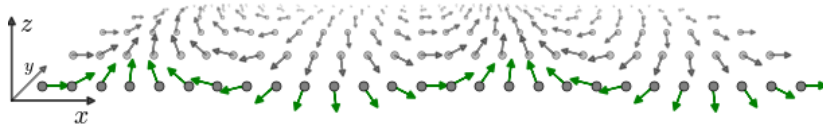


Figure 3: Illustration of a spin cycloid evolving along the x-axis. Each arrow represents an atomic spin vector.

As we want to compare the energy of the discrete system with the continuum model functionals, we need PBC to be satisfied in the definition of the structure. Indeed, since we are using PBC in the computation of the spin Hamiltonian, a structure mismatch at the system borders would negatively affect the comparison between such Hamiltonian and the energy functional. Being $L \simeq na$ the

¹⁰As specified in [5], a structure defined as in Eq. (33) corresponds to an energy minimum only in the case of zero anisotropy. For a more detailed discussion see Ch. 3.

system size, with n number of atoms per side and a lattice constant, we choose $\lambda = L/2$ (as shown in Fig. 3). Note that the structure shape is independent of the value of L . In the discrete model, this is equivalent to state that L is constant while a varies, $a \propto 1/n$. We discretize the cycloid function over a $n \times n$ lattice and we numerically evaluate the energy components. A comparison between the discrete system energies and the energy functionals is shown in Fig. 6.

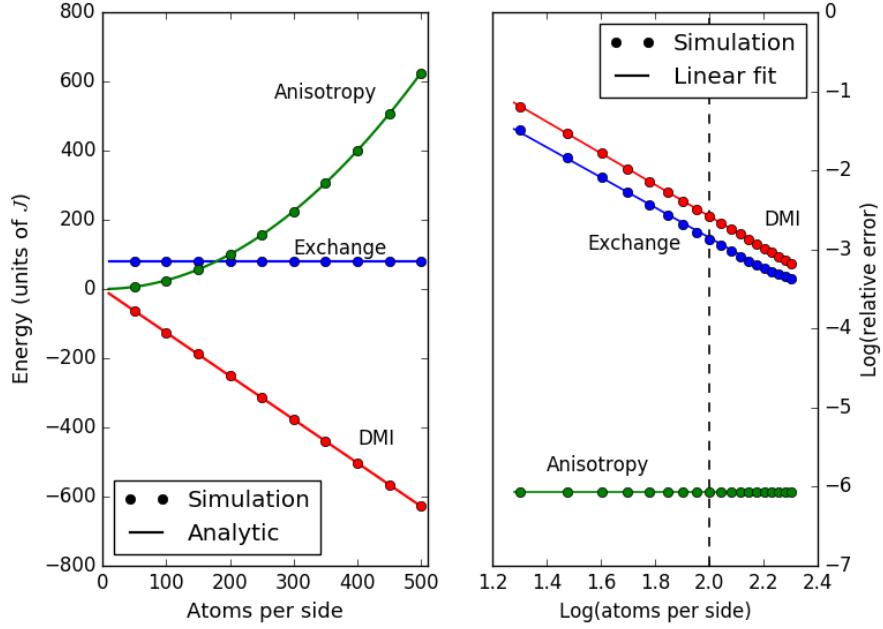


Figure 4: Left: plot showing the dependence of the different energy components (represented in units of J) on the number of atoms per side, both for the discrete system and continuum model. Right: bilogarithmic (base 10) plot showing the dependence of the relative error between the spin Hamiltonians and the rescaled continuum-model functionals on the number of atoms per side. The vertical line corresponds to the number of atoms per side that will be used in future simulations. Parameters values: $D = 0.1J$, $K = 0.01J$.

Referring to Table 1, we can note that ε_{ex} does not depend on a , while ε_{an} depends on $1/a^2 \propto n^2$ and ε_{DM} depends on $1/a \propto n$. This is exactly the behavior observed in the (left) plot, both for the discrete system and the continuum model.

As next step, we consider rescaled energy functionals ($\tilde{\varepsilon}$), so that to avoid the dependence on n , in order to check how these compare with the rescaled discrete-system energies ($\tilde{\mathcal{H}}$). In detail, we have

$$\begin{array}{c|c}
\mathcal{H}_{ex} = \tilde{\mathcal{H}}_{ex} & \varepsilon_{ex} = \tilde{\varepsilon}_{ex} \\
\mathcal{H}_{an} = n^2 \cdot \tilde{\mathcal{H}}_{an} & \varepsilon_{an} = n^2 \cdot \tilde{\varepsilon}_{an} \\
\mathcal{H}_{DM} = n \cdot \tilde{\mathcal{H}}_{DM} & \varepsilon_{DM} = n \cdot \tilde{\varepsilon}_{DM}
\end{array}$$

We then compute the relative error $\delta = |\frac{\tilde{\mathcal{H}} - \tilde{\varepsilon}}{\tilde{\varepsilon}}|$ and we represent it on a bilogarithmic plot. By computing the slope, we note that the relative error related to the exchange and the DMI decreases as n^{-2} , while the one related to the anisotropy stays constant. The reason of this latter behavior relies on the periodicity of the structure used and on the way it has been discretized. Indeed, as the anisotropy energy does not depend on the interaction among atomic spins but only on the absolute value of their z-components, few atoms per side are enough to make the energy converge to a fixed value. Such a value depends on how the system has been discretized.

	Continuum	$ \Delta $
Exchange	$7.896 \cdot 10^1$	$1.057 \cdot 10^{-1}$
Anisotropy	$2.500 \cdot 10^{-3}$	$2.110 \cdot 10^{-9}$
DMI	$-1.257 \cdot 10^1$	$3.308 \cdot 10^{-3}$

Table 2: Rescaled energy functionals (continuum) and absolute error ($|\Delta| = |\tilde{H} - \tilde{\varepsilon}|$) between these results and the rescaled energies numerically computed for the discrete system as obtained for a cycloid structure (Eq. (33)), all expressed in units of J , with $n = 100$, $D = 0.1J$ and $K = 0.01J$.

In the simulations performed in the following chapters, we will use $n = 100$. From Fig. 6 we observe that, with this number of atoms per side, we obtain a relative error close to 10^{-3} , in the case of exchange and DMI. We take this into account for future comparisons (Ch. 3) between discrete-system energies and corresponding functionals. Table 2 gives us information about the absolute error values with $n = 100$.

Considering the results obtained, we conclude that the discrete-system Hamiltonians introduced in Ch. 1 are the ones implemented in the UppASD. Moreover, we evaluated the discretization error we will encounter in future simulations.

2.2 Dynamics testing

In this section, we numerically compute the dispersion relation for a one-dimensional spin chain and we compare it with the analytical solution. The aim is to verify the integration of the LLG equation (in case of zero damping) and have an estimate of the time step needed to resolve the dynamics.

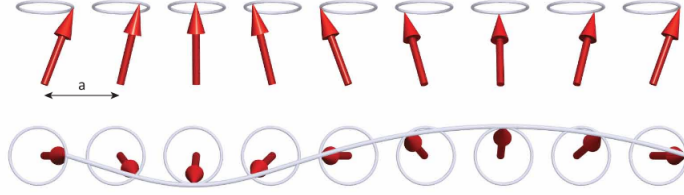


Figure 5: Representation of a spin wave in a one-dimensional spin chain (with lattice constant a), showing the precession orbits of the single atomic spins. Figure extracted from [32].

A spin wave is an excitation propagating in the form of atomic spins tilt with respect to the collinear configuration [43] (Fig. 5). As first step, we want to find the analytical expression of the dispersion relation for a spin wave propagating in a one-dimensional spin chain, whose energy is defined by the Hamiltonian $\mathcal{H} = \mathcal{H}_{ex} + \mathcal{H}_{an}$ (no DMI considered). Taking into account Eq. (28) and the previous Hamiltonian, we have

$$\mathbf{B}_p = \frac{J}{2}(\mathbf{m}_{p-1} + \mathbf{m}_{p+1}) - \frac{K}{2}\mathbf{e}_z. \quad (34)$$

The dynamics of each spin is described by Eq. (25). Our aim is to find a solution of the form

$$\begin{aligned} m_p^x &= ue^{i(pqa - \omega t)}, \\ m_p^y &= ve^{i(pqa - \omega t)}, \\ m_p^z &\simeq |\mathbf{m}|, \end{aligned}$$

where u and v are constants, q is the wave number, a the lattice constant and ω the precession frequency. By following a similar procedure as in [43], we find a solution for ω , given as

$$\omega = \gamma|\mathbf{m}|[J(1 - \cos qa) + \frac{\gamma K}{2}]. \quad (35)$$

In our case we have $|\mathbf{m}| = \mu_B$ and, by defining $K = \tilde{K}J$, \tilde{K} the dimensionless anisotropy constant, and, as previously, $J = \tilde{J}/\mu_B^2$, \tilde{J} with dimensions of energy,

we rewrite Eq. (35) in dimensionless units, as follows

$$\tilde{\omega} = (1 - \cos qa) + \frac{\tilde{K}}{2}, \quad (36)$$

with $\tilde{\omega} = \omega \mu_B / \gamma \tilde{J}$.

In order to compare the numerical results with the analytical ones, we consider a 50-atoms-long spin chain with PBC. We tilt each atomic spin following a discretized harmonic function, so that

$$\begin{aligned} \tilde{m}_p^x &= u \sin pq, \\ \tilde{m}_p^y &= v \cos pq, \\ \tilde{m}_p^z &= \sqrt{1 - u^2 - v^2}, \end{aligned} \quad (37)$$

with $p = 1, \dots, 50$ and $u^2 = v^2 = 10^{-2}$. The values that q can assume must let the structure meet PBC. Once the structure has been initialized, we start the dynamics. In order to extract the precession frequency of the atomic spins, we compute the discrete Fourier transform of an atomic spin's component¹¹. Fig. 6 shows the results obtained for three different values of \tilde{K} .

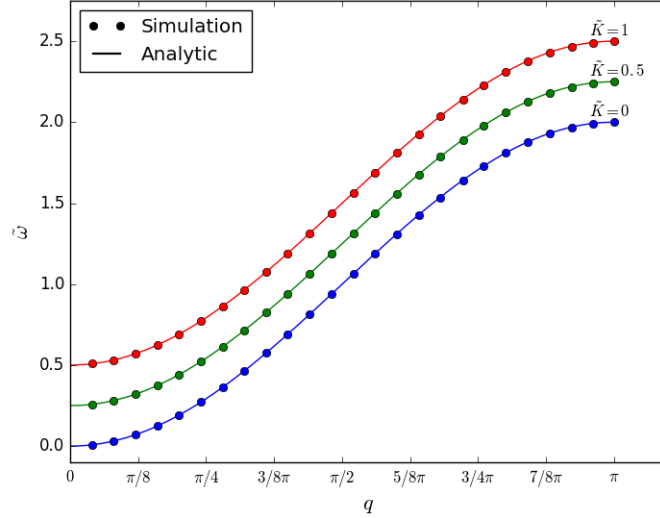


Figure 6: Plot showing the dispersion relation $\tilde{\omega}(q)$ for three different values of \tilde{K} , comparing the analytical result given in Eq. (36) and the numerical result obtained by using a 50-atoms-long chain, with an initial structure given by Eq. (37). Time step: $0.1 \cdot \Delta\tau_{step}$. Number of time steps: 10^5 . No damping.

The numerical integration has been evaluated by using $\Delta\tau = 0.1 \cdot \Delta\tau_{step}$ (time step) and $N_\tau = 10^5$ (number of steps), for all \tilde{K} values. These parameters

¹¹See App. B.1 for further details.

are important for the correct evaluation of the precession frequency and for the accuracy of the dynamics. Indeed, in order to correctly evaluate $\tilde{\omega}$ for all adopted values of q and \tilde{K} , we must have

$$\begin{aligned}\tilde{\omega}_{max} \cdot \Delta\tau &\ll 1, \\ N_\tau \cdot \tilde{\omega}_{min} \cdot \Delta\tau &\gg 1,\end{aligned}\tag{38}$$

where $\tilde{\omega}_{max}$ is the highest precession frequency ($\tilde{\omega}_{max} = 5/2$) and $\tilde{\omega}_{min}$ the smallest one (obtained with $\tilde{K} = 0$ and $q = 2\pi/50a$). From Eq. (36), we have

$$\begin{aligned}\tilde{\omega}_{max} \cdot \Delta\tau &= 0.022, \\ N_\tau \cdot \tilde{\omega}_{min} \cdot \Delta\tau &\simeq 7.\end{aligned}$$

Thus, the values of $\Delta\tau$ and N_τ used satisfy Eq. (38). In future simulations, the highest value of \tilde{K} adopted will be on the order of 0.1. App. B.2 shows the error analysis for the dispersion relation for such a \tilde{K} , with two different values of $\Delta\tau$.

In conclusion, we have observed how the numerical results well match the analytical predictions, giving us confidence about the correct integration of the LLG in the UppASD. Moreover, we found the order of magnitude for $\Delta\tau$ that guarantees a sufficiently accurate description of the dynamics, in relation with the interaction parameters adopted.

3 Phase diagram

In this chapter, we examine how the energy of a cycloid structure and a Néel-type skyrmion compares with the energy of the uniform ferromagnetic (FM) state in a 100-atoms-per-side discrete system, while tuning the anisotropy (K) and the DMI parameter (D). In particular, we observe how the system finite size, periodic boundary conditions (PBC) and the structure relaxation affect the result. The aim is to obtain a phase diagram for the system at hand and, where possible, compare it with analytical results.

3.1 Cycloid phase diagram

In this section, we investigate how the spin cycloid total energy compares with the FM state energy while tuning the values of K and D . We first introduce the analytical results obtained by using open boundary conditions (OBC), periodic boundary conditions (PBC) and by studying the domain wall energy. Later, we compute the numerical results, with and without structure relaxation, and we compare them with the analytical results.

As first step, we consider the analytical representation of the spin cycloid, as given by Eq. (33), and we find the value of the cycloid wavelength λ that minimizes the total energy functional $\varepsilon = \varepsilon_{ex} + \varepsilon_{an} + \varepsilon_{DM}$ for a square sample of size $L = 100a$ (in the discrete system representation, 100 atoms per side). This calculation has been performed considering OBC. Therefore, there are no constraints in the values λ can assume. Comparing the energy functional with the FM state energy ($= -2NJ$, $N = 10^4$), we obtain the following relation between K and D (for a more detailed description about the result found, see App. C):

$$D = \sqrt{\frac{K}{2}}. \quad (39)$$

This result is indicated in Fig. 8 with the dashed line.

As second step, we compute the value of λ that minimizes the previous energy functional for the same sample, this time taking into account PBC. Thus, the optimal λ can assume only discrete values. In the range of K and D considered, the optimal λ corresponds to three values: $\lambda_1 = 100a$, $\lambda_2 = 50a$ and $\lambda_3 = 100/3a$. Again, we substitute them in ε and we compare the total energy functional with the FM state energy. The result is displayed with colored solid lines in Fig. 8.

As third step, we consider the solution found in [5], obtained by studying, in a continuum model, the domain wall energy in a one-dimensional infinite system and by comparing its energy with the FM state energy. A cycloid structure can be seen as a succession of several domain walls whose domain wall width depends on the value of the cycloid wavelength. Moreover, the solution found for a one-dimensional system can be extended to a two-dimensional one, as the domain wall is uniform in the second dimension. Furthermore, when the domain wall width is small compared to the system size, the energy contribution stems

only from a restricted region in space and is hardly affected by the boundary conditions. In this situation, it is possible to consider the solution relative to a domain wall in an infinite one-dimensional system, given by¹²

$$D = \frac{2}{\pi} \sqrt{K}. \quad (40)$$

This relation is indicated by the dashed-dotted line in Fig. 8. In order to relate the numerical results with the analytical solutions found, we discretize the spin cycloid, as done in Sect. 2.1, and we compare the total energy of the system with the FM state energy (for a given value of K , we tune D till the energy of the system equals the FM state energy), using the optimal values of λ found in the previous analysis with PBC. We find good agreement between the numerical results obtained (open circles in Fig. 8) and the analytical results discussed before¹³.

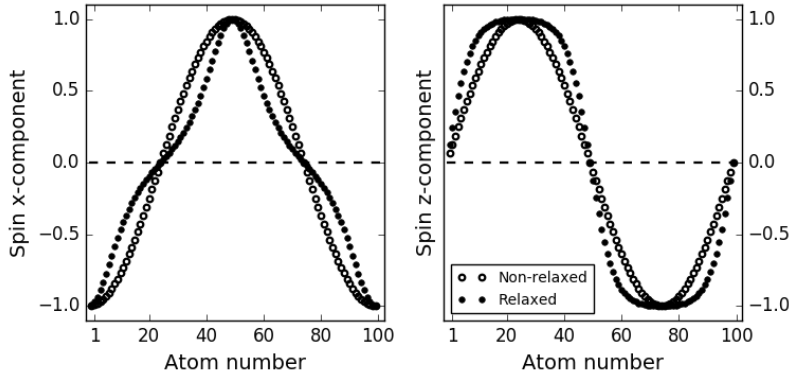


Figure 7: Plots showing the x -components (left) and the z -components (right) of the atomic spins in a 100-atoms-per-side cycloid structure with wavelength λ_1 , before and after relaxation. The dynamics is evaluated with $K = 0.015J$ and $D = 0.091J$, which corresponds to the highest anisotropy solution shown in Fig. 8 for the non-relaxed structure with wavelength λ_1 (time step: $\Delta\tau_{step}$, total integration time: $10^4 \cdot \Delta\tau_{step}$, damping parameter: 0.1).

The previous considerations have been made not taking the dynamic evolution into account but by merely computing the energy of the discretized system. By letting the dynamics evolve, it can be noticed that the cycloid structure reshapes in a more stable configuration (still cycloid-like) while the total energy

¹²The D_c expression is slightly different as the one given in [5], as we take into account the energy parameter rescaling as given by Table 1 and the relation is written in units of J .

¹³We must take into account that a discretization error, as evaluated in Sect. 2.1, always affects the numerical results.

reduces. This is due to the fact that Eq. (33) describes a stable cycloid structure only in the zero-anisotropy case, while a finite anisotropy modifies the function shape, as explained in [5]. Fig. 7 shows how the relaxation affects the cycloid with wavelength λ_1 . It can be seen that the relaxed configuration has steeper walls, making the anisotropy energy of the system lower and making the structure resemble more a sequence of domain walls.

As next step, we compare the energy of the relaxed structures (after a relaxation time of $10^4 \cdot \Delta\tau_{step}$) with the FM state energy, still using the optimal wavelengths λ_1 , λ_2 and λ_3 , and in the same range of K and D . The cycloid energy decreases for all values of λ considered and the “cycloid region” in the phase diagram increases. Moreover, in the region analyzed, the relaxed cycloid with wavelength λ_1 has always an energy lower than the energies of the relaxed cycloids with different wavelength¹⁴.

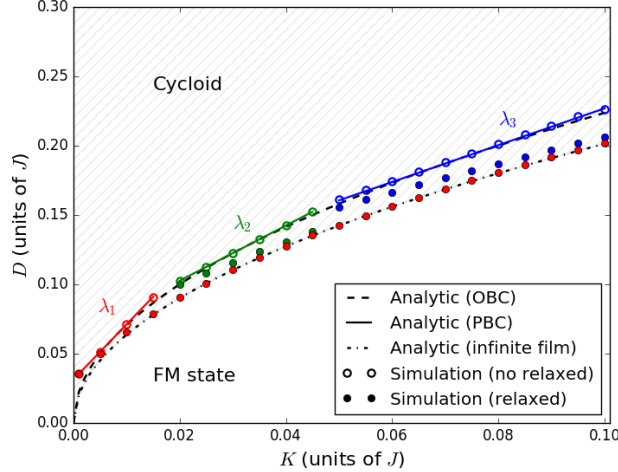


Figure 8: Phase diagram of the cycloid structure and FM state. The dashed line represents the analytic solution found using OBC, as given in Eq. (39). The dashed-dotted line represents the analytic infinite film solution as given in Eq. (40). The continuum lines represent the solution found considering PBC. The empty circles represent the same solution found in the discrete model. The full circles represent the solution found in the discrete model by letting the system relax (time step: $\Delta\tau_{step}$, total integration time: $10^4 \cdot \Delta\tau_{step}$, damping parameter: 0.1).

Considering the phase diagram plot, we note a good match between the analytical and numerical results relative to the non-relaxed structure with PBC (empty circles and continuum lines). We observe that all solutions relative to the relaxed structure converge to Eq. 40 and, in particular, the structure relative to

¹⁴We also analyzed which wave vector direction minimizes the relaxed cycloid energy. We found that the wave vector directed along the x-axis (or, equally, the y-axis) has the lowest energy.

λ_1 matches better (full red circles). This is due to the fact that, according to the analysis in [5], the analytical result optimal width Δ decreases as K increases ($\Delta \propto \sqrt{1/K}$). As described previously, the reshaped cycloid structure resembles adjacent domain walls, whose domain width depends on the value of λ chosen (due to PBC). In particular, a high value of λ can let the structure have wider walls. Thus, the structure relative to λ_1 matches better with the analytical solution (compared to structures relative to λ_2 and λ_3) and this match becomes worse as K decreases. Indeed, for the smallest K values observed, Δ is too wide to fit in the finite system, even for the structure relative to λ_1 . Moreover, as K decreases, the relaxed structure shape gets closer to a cycloid function, thus making the comparison with the domain wall less adequate.

In conclusion, we have computed the phase diagram for a cycloid structure in a 100-atoms-per-side system. We have seen that, taking into account PBC and the structure relaxation, the cycloid relative to $\lambda_1 = L$ has the lowest energy for the interaction parameters investigated. We have compared numerical and analytical results and we have observed a good match between them, both for the non-relaxed and relaxed structure.

3.2 Skyrmion phase diagram

In this section, we numerically investigate how the energy of the Néel-type skyrmion structure compares with the energy of the FM state while tuning K and D in the same range as done for the cycloid structure. The aim is to compute a phase diagram for such a skyrmion and compare this to the region in which the spin cycloid is the ground state.

A Néel-type skyrmion is a magnetic structure with radial symmetry that can be stabilized by the DMI [44] and in which atomic spins, going from the core outwards, rotate in the radial planes, as shown in Fig. 9.

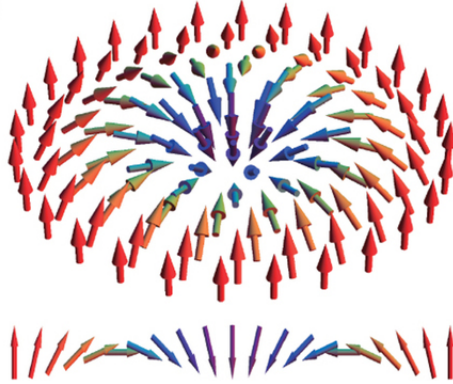


Figure 9: Illustration of a Néel-type skyrmion (top) together with the cross section through the origin (bottom). Figure extracted from [45].

In order to compare the skyrmion energy with the FM state energy, we

introduce a skyrmion-like structure in our discrete model (100 atoms-per-side, as in the previous analysis). To do so, we consider the analytical expression given by [5], which is an adaptation of the domain wall for a radially symmetric structure, and we discretize such a function. The function reads as follows:

$$\theta(r) = 2 \arctan[\exp(\frac{r-R}{\Delta})] + \pi, \quad (41)$$

where $\theta(r)$ is the angle between the z-axis and the atomic spin vector located at distance r from the centre of the structure, Δ is the domain wall width defined previously and R is the skyrmion radius.

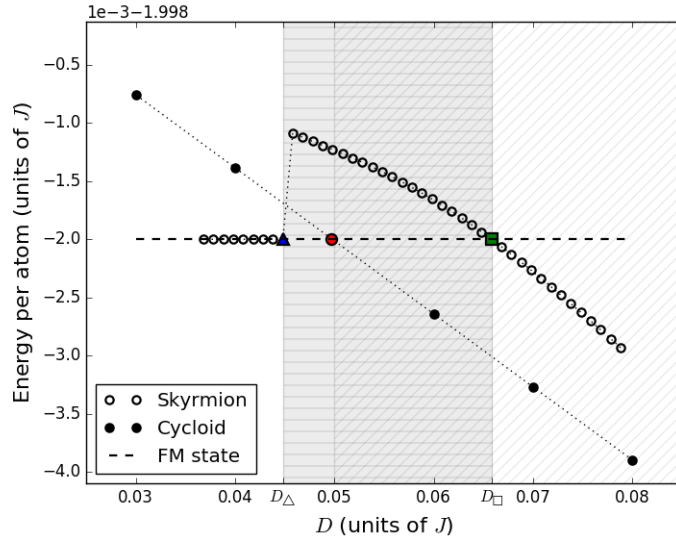


Figure 10: Plot showing the energy of the relaxed skyrmion (empty circles) and the relaxed cycloid (filled circles) in relation with D , for $K = 0.005J$. D_Δ and D_\square define the skyrmion metastability region with respect to the FM state. Relaxation parameters for both structures are defined in the text.

For each given value of K , we start with a discretized configuration as given by Eq. (41), with $R = 20$, and a high enough value of D to make the skyrmion structure stable. We then let the structure relax¹⁵. We decrease the value of D of a quantity $D_{step} = 0.001J$ and, again, we let the system relax and we compute the energy. We carry on this procedure till the structure degenerates into a FM state. In order to provide a better description on how the phase diagram has been obtained, we show the energy values of the relaxed structures

¹⁵For the first relaxation, we use a time step of $\Delta\tau_{step}$, a total integration time of $5 \cdot 10^4 \cdot \Delta\tau_{step}$ and a damping parameter of 0.1. For following relaxations, we decrease the total integration time to $3 \cdot 10^4 \cdot \Delta\tau_{step}$.

in relation with D , for a given K . Fig. 10 shows the results for $K = 0.005J$. From the plot, we can identify the skyrmion metastability range, defined by the value of D in which the skyrmion energy overcomes the FM state energy (D_{\square}) and the value of D in which the skyrmion becomes unstable (D_{\triangle}). This is further compared with the energy of the relaxed spin cycloid obtained in the previous section (thick dots). The red dot indicates the energy at which the spin cycloid becomes metastable with respect to the FM state. Since this falls within the region where the skyrmion is already metastable, we learn that the cycloid energy is always lower than the energy of the skyrmion. The metastability range is shown in Fig 11.

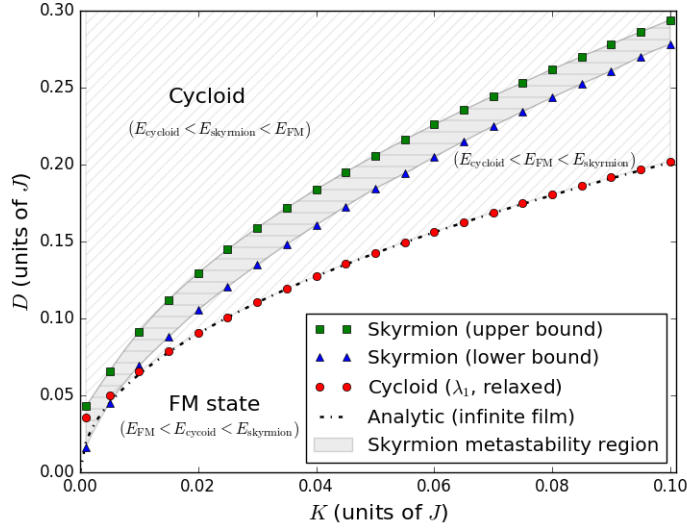


Figure 11: Plot showing the phase diagram of the skyrmion and cycloid structure. Squares and triangles delimit the relaxed skyrmion metastability region compared with the FM state in a discrete system, as shown in Fig. 10 (initial configuration and relaxation parameters described in the text). Full dots represent the solution of the relaxed cycloid with wavelength λ_1 , as described in the previous section. The dashed and dotted line represents the analytical infinite film solution as given in Eq. (40).

The analytical solution relative to an infinite film is the same as the one for the cycloid state (Eq. (40)). This is due to the fact that, in case of an infinite film, the skyrmion radius R diverges when its energy approaches the energy of the FM state and, thus, curvature energy costs are negligible. In particular, the solution found is valid when $R \gg \Delta$, with Δ domain wall width. In our situation, this is not the case for high values of K . We note that for small values of K a better match is achieved. Future works may consider a more detailed analysis about the influence of finite sizes on the skyrmion radius in its metastability region and how it compares with Δ .

In conclusion, we have computed a phase diagram that shows the Néel-type skyrmion metastability region with respect to the FM state for the discrete system considered. We also find that the skyrmion is always metastable with respect to the cycloid structure, while its energy can be below the FM state energy for sufficiently large D .

4 Switching between magnetic structures

In the previous chapter, we have detected a metastability region for the skyrmion structure with respect to the FM state. In this last chapter, we use these previous results to study the conditions in which it is possible to obtain a ‘switch’ from a skyrmion structure to a FM state by suddenly changing the DMI parameter value. Physically, this might be realized by optical excitation of strain waves in multilayer structures [46], such that the interface is lifted for a short period of time, which in turn can induce a transient change of the DMI parameter. First, our aim is to find the parameter range under which such switching is feasible by relatively small changes of the DMI parameter. Second, we investigate a wider range of changes in the DMI parameter leading to a modification of the skyrmion chirality.

4.1 Skyrmion to FM state switching

In this section, we study how a step-like change in the D value can make a skyrmion structure evolve to a FM state. Starting from a relaxed skyrmion structure corresponding to a given value of D and K , we first observe how the system energy changes in time for different values of the induced change ΔD and how the energy and the structure itself evolve during the switch. Secondly, for a given value of K , we compute a diagram showing the value of ΔD needed in order to obtain a switch, in relation with the initial D value.

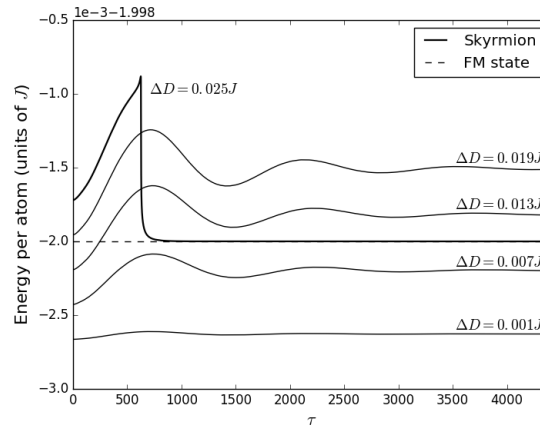


Figure 12: Plot showing the dynamical evolution of the energy per atom, given in units of J , with respect to the dimensionless time parameter τ (see Eq. (29)), for several perturbations of D . For all cases, the initial skyrmion structure is the relaxed structure corresponding to $D_i = 0.0758J$ and $K = 0.005J$ (computed in the same way as in Fig. 10). Each solid line corresponds to a different value of D_f , $D_f < D_i$, with $\Delta D = |D_f - D_i|$. The dashed line indicates the energy of the FM state. Time step: $\Delta\tau_{step}$, total integration time: $5 \cdot 10^4 \Delta\tau_{step}$, damping parameter: 0.1.

We start by taking into account the results shown in Fig. 10. By using the same value of K and considering the relaxed skyrmion structure for $D_i = 0.0758J$, we study how the skyrmion energy dynamically evolves if the value of D is suddenly changed to D_f , $D_f < D_i$. Thus, we observe several energy evolutions while tuning $\Delta D = |D_f - D_i|$. The results are shown in Fig. 12. By increasing ΔD , we observe that the skyrmion, which is initially stable (energy lower than FM state), becomes metastable and, when ΔD is large enough, the energy suddenly drops and stabilizes to a value equal to the FM state energy.

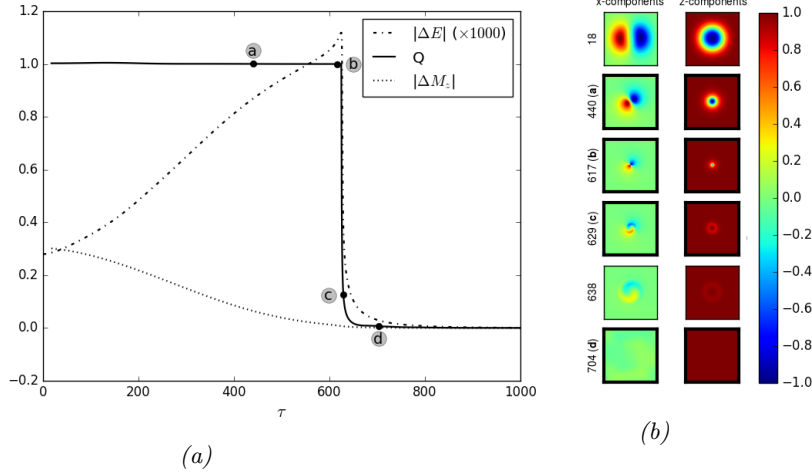


Figure 13: (a): plot showing the dynamic evolution of three distinct quantities during a skyrmion-to-FM state switch, with $D_i = 0.0758J$ and $\Delta D = 0.025J$: $|\Delta E(t)| = |E(t) - E^{FM}|$ is the absolute value of the difference between the energy per atom of the FM state and the current structure (in units of J , multiplied by a factor 1000), Q is the value of the topological charge of the current structure and $|\Delta M_z(t)| = |M_z(t) - M_z^{FM}|$ is the absolute value of the difference between the total magnetization along the z -axis per atom of the FM state and the current structure. Time step: $\Delta\tau_{step}$, total integration time: $2 \cdot 10^4 \Delta\tau_{step}$, damping parameter: 0.1. (b): dynamics of the spin texture showing the annihilation of the skyrmion into the FM state. The highlighted samples correspond to the symbols a-d in (a). Labels on the left side show the time each texture plot refers to. The colorbar on the right gives information about the value assumed by the two components in the texture plots.

In order to have a better description of the dynamical evolution in the situation where the switch is observed, together with the system energy we plot the total magnetization along the z -axis and the topological charge Q , an integer number that topologically characterizes a magnetic structure, which, for a

continuum model¹⁶, is defined as

$$Q = \frac{1}{4\pi} \int \tilde{\mathbf{m}} \cdot \left(\frac{\partial \tilde{\mathbf{m}}}{\partial x} \times \frac{\partial \tilde{\mathbf{m}}}{\partial y} \right) dx dy, \quad (42)$$

where $\tilde{\mathbf{m}}$ is the unit vector determining the atomic spin direction (see, for instance, Eq. (29) and Eq. (33)). The result is shown in Fig. 13-a. A stable skyrmion is characterized by $Q = 1$. We see that, initially, Q remains close to one and then abruptly decays to zero, which is the value corresponding to a FM state, in the same moment when the energy drop is observed. The magnetization, on the other hand, experiences a smoother transition. Fig. 13-b shows the structure evolution for the same switch. We notice that the skyrmion radius continuously decreases until it completely disappears. In addition, from the dynamics of the x-components, we observe an anti-clockwise rotation. Moreover, we see that the finite dimensions of the sample do not seem to affect the dynamics, as the skyrmion radius is always much smaller than the system size. Considering the results shown in the previous figures, we note that a time value of 704 is required, in this situation, to experience a complete switch. Naturally, this switching time is dependent on the D_i chosen. We expect that, the closer D_i is to D_Δ (see Sect. 3.2) the lower this switching time is. We may assume that the lowest value of switching time achievable corresponds to the time needed for the Q value to drop. Referring to Fig. 13, we see that such a time corresponds to a value of about 100. Further analysis about the dependence of the switching time on D_i , as well as on the anisotropy parameter K and the damping parameter α , is needed in order to optimize it.

As final step, we want to compute, for $K = 0.005J$, a diagram showing the lowest value of ΔD needed to experience a skyrmion-to-FM state switch in relation with D_i . To do so, for each value of D_i , we start with the corresponding relaxed skyrmion structure (as computed in the previous chapter, see Fig. 10) and we let the structure relax again for increasing values of ΔD (thus, decreasing D_f). We record the value of ΔD for which a switch happens. Results are shown in Fig. 14. We note that, for values close to D_Δ , data are slightly scattered. This is due to the choice of the smallest value of ΔD chosen to generate the plot. Performing a linear fit, we obtain the following relation

$$\Delta D = c(D_i - D_\Delta), \quad (43)$$

with $c = 0.761$ and $D_\Delta = 0.0458J$. As expected, for D_i close to D_Δ , only a small ΔD is required to observe a switch, since the skyrmion is already metastable with respect to the FM state. Taking into account Fig. 10, we would expect that a value of ΔD equals to $D_i - D_\Delta$ is needed to observe a switch. Since in Eq. (43) we have $c < 1$, we understand that this is not the case, but a smaller ΔD is sufficient for a switch to happen. This might be due to the energy oscillations the system experiences when the DMI parameter is changed, as shown in Fig. 12, which destabilize the skyrmion structure.

¹⁶See App. D for details about implementation in a discrete model.

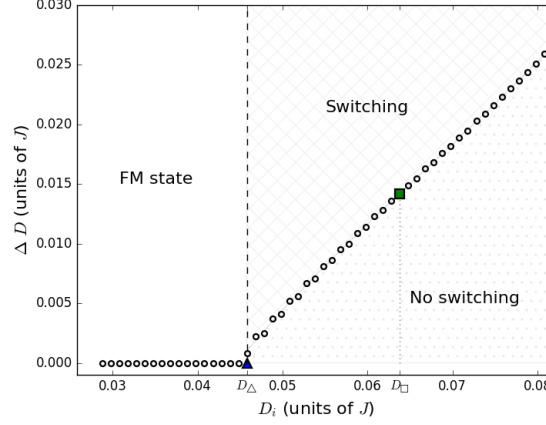


Figure 14: Plot showing the lowest value of ΔD in which a skyrmion-to-FM state switch is observed in relation with D_i , which defines the initial skyrmion structure (as described in the text).

In conclusion, we have seen that it is possible to switch from a skyrmion structure to a FM state by a sudden change of the DMI parameter. We have observed that, in this situation, the value of the topological charge drops on a timescale much shorter compared to the total time needed to reach the FM state. Moreover, we have seen that the minimum value of ΔD required in order to observe a switch is 0.761 times smaller than expected from the equilibrium phase diagram.

4.2 Skyrmion chirality switching

In the previous section, we have detected the minimum value of ΔD needed to experience a skyrmion-to-FM state switch, for a given value of K and different values of D_i . In this section, we show that, for very high values of ΔD , it is possible to go from one skyrmion structure to another one with opposite chirality. Interestingly, despite the large change in the DMI parameter, the evolution shows that this happens without the passage through the FM state.

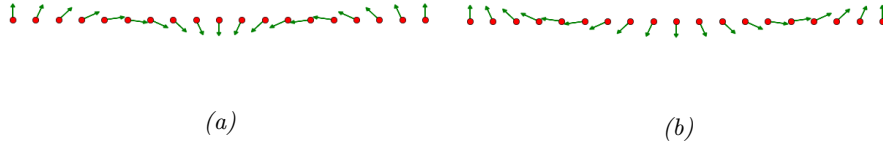


Figure 15: Illustrations of Néel-type skyrmion cross sections with opposite chirality.

In this situation, we refer to skyrmion chirality as the orientation the atomic spins follow while going from the skyrmion centre outwards. Being the structure radially symmetric, there are two ways the spins can tilt, as shown in Fig. 15. This definition of chirality resembles the domain wall chirality [5] where, instead of a domain wall structure, we are considering the skyrmion cross section. We start by considering the relaxed skyrmion structure relative to $K = 0.005J$ and $D \equiv D_i = 0.0758J$, as done in the previous section. We again suddenly change the value of D to $D_f = -0.0800J$, thus $\Delta D = 0.1558J$. Note that D_f is now negative. We let the structure evolve and we compute the total energy, the topological charge Q and the total magnetization along the z-axis and we plot them as function of time. The result is shown in Fig. 16. We note that the topological charge experiences a sudden peak and returns to a value of 1, indicating that the structure after relaxation still resembles a skyrmion. The energy and magnetization values experience oscillations. Fig. 17 shows the time evolution of the x-components and z-components of the structure. We note that the final structure is indeed a skyrmion, with the x-components ‘mirrored’ with respect to the initial structure, as illustrated in Fig. 15. We argue that the reason for this change is due to the fact that the sign of D defines the chirality of the skyrmion, thus the orientation the spins must follow in order to lower the DMI energy. For example, the analytical structure defined by Eq. (41) makes the skyrmion have a negative DMI energy for positive values of D . The chirality can be inverted by considering a different function, such as

$$\theta(r) = 2 \arctan[\exp(-\frac{r-R}{\Delta})] + 2\pi. \quad (44)$$

It can be analytically shown that such expression gives a negative DMI energy for negative values of D .

The magnetic structure evolution shows two important aspects. First, from texture plots in Fig. 17, we observe that energy oscillations directly relate to oscillations of the skyrmion structure. This indicates that the dynamics proceeds by excitation of skyrmion zero modes. Second, we observe that the dynamics is strongly affected by the finite system size. Future studies at larger system size and with different boundary conditions are needed to investigate the role of the periodic boundary conditions in the switching between skyrmions of different chirality. Finally, by observing the texture plots, we note that, within a time value of 704, the new structure resembles already a skyrmion. Thus, we can argue that this is the time needed for the chirality switch to happen. Note that such a time is the same as the one identified for the skyrmion-to-FM state switch in the previous section.

In conclusion, we have analyzed the possibility to switch the skyrmion chirality by applying a large change of the DMI parameter. We have found an analytical explanation for such a switch and we have observed how the dynamics is affected by the system size and boundary conditions. Moreover, we have estimated the time scale in which such a switch happens and we have found a correlation between the skyrmion size and the energy oscillations the system experiences.

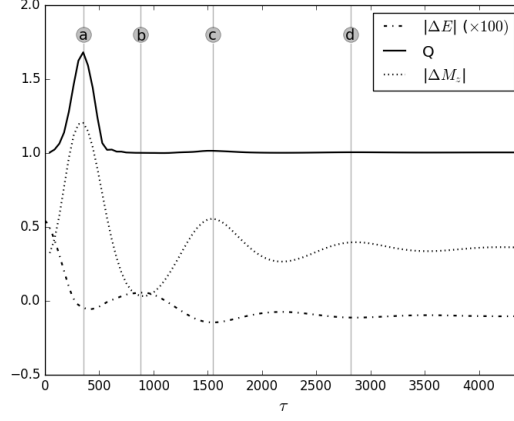


Figure 16: Plot showing the dynamics of three distinct quantities during the skyrmion chirality-switch, with $D_i = 0.0758J$ and $\Delta D = 0.1558J$: $|\Delta E(t)| = |E(t) - E^{FM}|$ is the absolute value of the difference between the energy per atom of the FM state and the current structure (in units of J , multiplied by a factor 100), Q is the value of the topological charge of the current structure and $|\Delta M_z(t)| = |M_z(t) - M_z^{FM}|$ is the absolute value of the difference between the total magnetization along the z -axis per atom of the FM state and the current structure. Time step: $\Delta\tau_{step}$, total integration time: $2 \cdot 10^4 \Delta\tau_{step}$, damping parameter: 0.1. The symbols a-d correspond to the texture plots in Fig. 17.

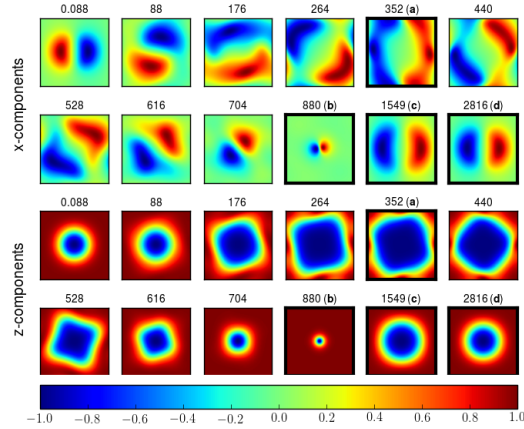


Figure 17: Texture plot showing the dynamics of the skyrmion chirality switch. The highlighted samples correspond to the symbols a-d in Fig. 16. Labels on the top show the time each texture plot refers to. The colorbar on the bottom gives information about the value assumed by the two components in the texture plots.

5 Concluding remarks

In this thesis, we have analyzed the behavior of cycloids and skyrmions in a two-dimensional system. Concerning the stability of these structures (Ch. 3), we have found two important aspects. First, the existence of a metastability region for the skyrmion structure with respect to the FM state. Second, the fact that a cycloid has always an energy lower than the skyrmion. Possible new studies might involve an investigation about how a finite temperature influences the phase diagram obtained.

Concerning the dynamical evolution (Ch. 4), we have demonstrated that a step-like modification of the DMI parameter can annihilate the skyrmion structure. We have found that the actual switching time, as defined by the time at which the topological charge disappears, happens on a timescale of about $1/7$ of the total time needed to reach the FM state. This suggests that the conservation of the topological charge is not the limiting factor for the switching process. In a future analysis, it would be worth to investigate the possibility to obtain a skyrmion annihilation by applying a DMI parameter ‘pulse’, which would resemble a behavior physically closer to what is experimentally feasible. Moreover, in order to achieve a full control of the skyrmion structure, the possibility to nucleate a skyrmion must be investigated.

Finally and unexpectedly, by applying a large change of the DMI parameter, we have demonstrated switching of the skyrmion chirality. This result suggests an alternative concept for memory devices, where the information unit is not given by the presence or absence of skyrmion structures but, instead, by the chirality that each skyrmion expresses.

Appendices

A UppASD input files and codes

In the following, we show examples of the input files used for our simulations. A link that directs to a GitHub repository containing some useful scripts is displayed at the end of the section. This is meant to facilitate a possible reproduction of the results obtained and to simplify the development of further analysis.

Main input file:

```
simid test2d00
ncell      100      100      1
BC         P       P       0
cell       1.00000  0.00000  0.00000
           0.00000  1.00000  0.00000
           0.00000  0.00000  1.00000
NAtoms     1
NTypes     1
Sym        2

posfile    ./posfile
momfile    ./momfile
exchange   ./jfile
anisotropy ./kfile
dm         ./dmfile

restartfile ./restartfile.dat

SDEalgh    1

initmag    4

temp       0

damping    0.1
Nstep      1000
timestep   1E-12

avrg_step  1
do_tottraj Y
tottraj_step 1000

do_prnstruct 1
```

```
plotenergy      1
```

Exchange interaction input file ($\tilde{J} = 2.127 \cdot 10^{-3} mRy$):

```
1 1  1.000      0.0      0.0      2.127162E-03
```

DMI input file ($D = 10^{-1} J$):

```
1 1  1.0  0.0  0.0  0.0      -2.127162E-04  0.0
1 1 -1.0  0.0  0.0  0.0       2.127162E-04  0.0
1 1  0.0  1.0  0.0  2.127162E-04  0.0      0.0
1 1  0.0 -1.0  0.0 -2.127162E-04  0.0      0.0
```

Anisotropy input file ($K = 10^{-1} J$):

```
1  1  -2.127162E-04  0.000  0.0  0.0  1.0  0
```

GitHub repository link: https://github.com/teostiff/UppASD_scripts.git.

B Dynamics testing

B.1 Discrete Fourier transform

In Sect. 2.2, we numerically compute the dispersion relation for a 50-atoms spin chain. Hereby, we explain how we calculate the frequency values.

We extract the time dependence from one of the transverse components of an atomic spin, expressed as a_m , $m = 0, \dots, N_\tau - 1$, and, by using the NumPy Python package [47], we compute the discrete Fourier transform (DFT) on it, defined as follows

$$A_k = \sum_{m=0}^{N_\tau-1} a_m \exp \left\{ -2\pi i \frac{mk}{N_\tau} \right\}, \quad k = 0, \dots, N_\tau - 1,$$

where N_τ is the number of time steps adopted. A single-frequency component can be represented by a complex exponential

$$a_m \sim \exp \{ i\tilde{\omega} m \Delta\tau \},$$

where $\Delta\tau$ is the time step between a_m and a_{m+1} . The frequency $\tilde{\omega}$ is extracted by observing at which k -value the real part of A_k shows a peak. Being \hat{k} such a value, we have

$$\tilde{\omega} = \frac{2\pi\hat{k}}{N_\tau\Delta\tau}.$$

A cosine (or sine) function can be represented by linear combination of complex exponentials with opposite frequency. Thus, in our case, we observe two distinct peaks. We always consider the one corresponding to a positive frequency. As in each DFT computation we are dealing with a single-frequency signal with absence of non-numerical noise, we do not find the need to apply data windowing in our analysis [48].

B.2 Error analysis

In Sect. 2.2, we showed the dispersion relation for different values of \tilde{K} , computed using the same value of $\Delta\tau$. We now examine how this result changes by using two different time step values. Fig. 18 displays the results obtained.

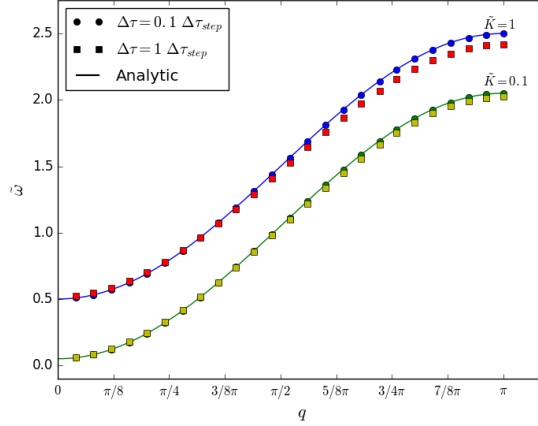


Figure 18: Plot showing the relation between $\tilde{\omega}$ and q for two different values of \tilde{K} , comparing the analytical result given in Eq. (35) and the numerical result obtained by using a 50-atoms-long chain, with an initial structure given by Eq. (37). Two different time step values used ($\Delta\tau$). Total integration time: $10^4 \cdot \Delta\tau_{step}$. No damping.

Our aim is to have an estimate of the dispersion relation error related with the precession frequency. In order to do that, two distinct values of anisotropy has been chosen: $\tilde{K}_1 = 1$, the highest anisotropy value taken into account in Sect. 2.2, and $\tilde{K}_2 = 0.1$, the highest anisotropy value used in Ch. 3. Considering the points relative to the highest frequency value ($q = \pi$), we compute the relative

error (η) for $\tilde{\omega}$ in the case of $\Delta\tau = 0.1 \cdot \Delta\tau_{step}$, with the “true” value being the analytical one ($\eta = |\tilde{\omega} - \tilde{\omega}^*|/\tilde{\omega}^*$, with $\tilde{\omega}^*$ analytical value). We have

$$\begin{aligned}\eta_1 &= 3.5 \cdot 10^{-2}, \\ \eta_2 &= 1.2 \cdot 10^{-2},\end{aligned}$$

where $\eta_{1,2}$ is the relative error corresponding to $\tilde{K}_{1,2}$. As expected, the error increases with the precession frequency, mainly because the accuracy of the time integration decreases while increasing the time step, especially when the dynamics is fast (high frequency).

We take this result into account when, in Ch. 3 and Ch. 4, we analyze the dynamics of more complex structures, but with the same time and energy parameters.

C Cycloid phase diagram

In the following, we show how we obtain Eq. (39). Considering the structure given in Eq. (33), we compute the energy functional $\varepsilon = \varepsilon_{ex} + \varepsilon_{an} + \varepsilon_{DM}$ by integrating on a square area of size $L = 100a$. We have

$$\varepsilon = \frac{20000\pi^2 J}{\lambda^2} + \frac{20000\pi D}{\lambda} + K[2500 + \frac{25\lambda \sin(\frac{200\pi}{\lambda})}{2\pi}].$$

By neglecting the harmonic term, we find the value of λ that minimizes the functional. We thus obtain

$$\lambda = -\frac{2\pi}{D},$$

where D is given in units of J . Substituting this value of λ in ε and making it equal to zero, we find the solution given by Eq. (39).

In order to find the solutions relative to PBC, we simply substitute λ_1 , λ_2 and λ_3 in ε and we find the relation between D and K that satisfies $\varepsilon = 0$.

D Topological charge

In Sect. 4.1 and Sect. 4.2 we compute the topological charge Q and we show its dynamic evolution. Hereby, we explain how this parameter has been calculated.

Following the description given in [6], we consider the expression:

$$Q = \frac{1}{4\pi} \sum_l A_l, \quad (45)$$

with

$$\cos(\frac{A_l}{2}) = \frac{1 + \mathbf{m}_i \cdot \mathbf{m}_j + \mathbf{m}_j \cdot \mathbf{m}_k + \mathbf{m}_k \cdot \mathbf{m}_i}{\sqrt{2(1 + \mathbf{m}_i \cdot \mathbf{m}_j)(1 + \mathbf{m}_j \cdot \mathbf{m}_k)(1 + \mathbf{m}_k \cdot \mathbf{m}_i)}}, \quad (46)$$

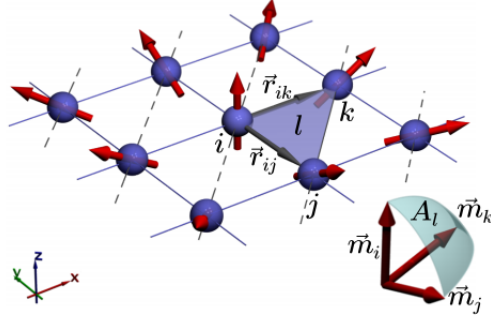


Figure 19: Illustration of a two-dimensional square lattice partitioned into elementary triangles, and spherical triangle A_l with vertices defined by atomic spins \mathbf{m}_i , \mathbf{m}_j , \mathbf{m}_k . Figure extracted from [6].

where l numbers all elementary triangles defined on the square lattice and A_l is the spherical triangle with vertices given by the atomic spins \mathbf{m}_i , \mathbf{m}_j , \mathbf{m}_k . The vertices i , j , k of each elementary triangle are numbered so that, being \hat{z} the versor defining the z -axis direction, we have $\hat{z} \cdot (\mathbf{r}_{ij} \times \mathbf{r}_{ik}) > 0$, where \mathbf{r}_{ij} is the vector connecting lattice site i to lattice site j (Fig. 19).

References

- [1] IBM 701 electronic analytical control unit. http://www-03.ibm.com/ibm/history/exhibits/701/701_1415bx01.html.
- [2] Tomasello, R. *et al.* A strategy for the design of skyrmion racetrack memories. *arXiv preprint arXiv:1409.6491* (2014).
- [3] Koshibae, W. *et al.* Memory functions of magnetic skyrmions. *Japanese Journal of Applied Physics* **54**, 053001 (2015).
- [4] Zhang, X. *et al.* Skyrmion-skyrmion and skyrmion-edge repulsions in skyrmion-based racetrack memory. *arXiv preprint arXiv:1403.7283* (2014).
- [5] Rohart, S. & Thiaville, A. Skyrmion confinement in ultrathin film nanostructures in the presence of dzyaloshinskii-moriya interaction. *Physical Review B* **88**, 184422 (2013).
- [6] Heo, C., Kiselev, N. S., Nandy, A. K., Blügel, S. & Rasing, T. Switching of chiral magnetic skyrmions by picosecond magnetic field pulses via transient topological states. *Nature Publishing Group. Scientific Reports* **6**, 27146 (2016).
- [7] Rößler, U., Bogdanov, A. & Pfleiderer, C. Spontaneous skyrmion ground states in magnetic metals. *Nature* **442**, 797–801 (2006).
- [8] Yu, X. *et al.* Near room-temperature formation of a skyrmion crystal in thin-films of the helimagnet fege. *Nature materials* **10**, 106–109 (2011).
- [9] Yu, X. *et al.* Real-space observation of a two-dimensional skyrmion crystal. *Nature* **465**, 901–904 (2010).
- [10] Mühlbauer, S. *et al.* Skyrmion lattice in a chiral magnet. *Science* **323**, 915–919 (2009).
- [11] Hsu, P.-J. *et al.* Electric-field-driven switching of individual magnetic skyrmions. *Nature Nanotechnology* (2016).
- [12] Liu, Y., Du, H., Jia, M. & Du, A. Switching of a target skyrmion by a spin-polarized current. *Physical Review B* **91**, 094425 (2015).
- [13] Sampaio, J., Cros, V., Rohart, S., Thiaville, A. & Fert, A. Nucleation, stability and current-induced motion of isolated magnetic skyrmions in nanostructures. *Nature nanotechnology* **8**, 839–844 (2013).
- [14] Mikhaylovskiy, R. *et al.* Ultrafast optical modification of exchange interactions in iron oxides. *Nature communications* **6** (2015).
- [15] Blundell, S. & Thouless, D. *Magnetism in condensed matter*, vol. 18 (Oxford university press New York, 2001).

- [16] Coey, J. M. *Magnetism and magnetic materials* (Cambridge University Press, 2010).
- [17] Mattis, D. C. *The theory of magnetism made simple* (World Scientific, 2006).
- [18] Shankar, R. *Principles of quantum mechanics* (Springer Science & Business Media, 2012).
- [19] Stevens, K. W. H. Exchange interactions in magnetic insulators. *Physics Reports* **24**, 1–75 (1976).
- [20] Liechtenstein, A., Katsnelson, M. & Gubanov, V. Exchange interactions and spin-wave stiffness in ferromagnetic metals. *Journal of Physics F: Metal Physics* **14**, L125 (1984).
- [21] Skriver, H. L. *The LMTO method: muffin-tin orbitals and electronic structure*, vol. 41 (Springer Science & Business Media, 2012).
- [22] Chikazumi, S. & Graham, C. D. *Physics of Ferromagnetism 2e*. 94 (Oxford University Press on Demand, 2009).
- [23] Cullity, B. D. & Graham, C. D. *Introduction to magnetic materials* (John Wiley & Sons, 2011).
- [24] Griffiths, D. J. *Introduction to quantum mechanics* (Cambridge University Press, 2016).
- [25] Dzyaloshinsky, I. A thermodynamic theory of “weak” ferromagnetism of antiferromagnetics. *Journal of Physics and Chemistry of Solids* **4**, 241–255 (1958).
- [26] Moriya, T. Anisotropic superexchange interaction and weak ferromagnetism. *Physical Review* **120**, 91 (1960).
- [27] Bode, M. *et al.* Chiral magnetic order at surfaces driven by inversion asymmetry. *Nature* **447**, 190–193 (2007).
- [28] Heide, M., Bihlmayer, G. & Blügel, S. Dzyaloshinskii-moriya interaction accounting for the orientation of magnetic domains in ultrathin films: Fe/w(110). *Physical Review B* **78**, 140403 (2008).
- [29] Crépieux, A. & Lacroix, C. Dzyaloshinsky–moriya interactions induced by symmetry breaking at a surface. *Journal of magnetism and magnetic materials* **182**, 341–349 (1998).
- [30] Bogdanov, A. & Hubert, A. Thermodynamically stable magnetic vortex states in magnetic crystals. *Journal of magnetism and magnetic materials* **138**, 255–269 (1994).

- [31] Stöhr, J. & Siegmann, H. C. Magnetism. *Solid-State Sciences. Springer, Berlin, Heidelberg* **5** (2006).
- [32] Mentink, J. *Magnetism on the timescale of the exchange interaction: explanations and predictions*. Ph.D. thesis, Radboud University (2012).
- [33] Hickey, M. C. & Moodera, J. S. Origin of intrinsic gilbert damping. *Physical review letters* **102**, 137601 (2009).
- [34] Oogane, M. *et al.* Magnetic damping in ferromagnetic thin films. *Japanese journal of applied physics* **45**, 3889 (2006).
- [35] Landau, L. & Lifshitz, E. On the theory of the dispersion of magnetic permeability in ferromagnetic bodies. *Phys. Z. Sowjetunion* **8**, 101–114 (1935).
- [36] Gilbert, T. A lagrangian formulation of the gyromagnetic equation of the magnetization field. *Phys. Rev.* **100**, 1243 (1955).
- [37] UppASD. <http://www.physics.uu.se/research/materials-theory/ongoing-research/uppasd/>.
- [38] Cellier, F. E. & Kofman, E. *Continuous system simulation* (Springer Science & Business Media, 2006).
- [39] Mentink, J., Tretyakov, M., Fasolino, A., Katsnelson, M. & Rasing, T. Stable and fast semi-implicit integration of the stochastic landau–lifshitz equation. *Journal of Physics: Condensed Matter* **22**, 176001 (2010).
- [40] Evans, R. F. *et al.* Atomistic spin model simulations of magnetic nanomaterials. *Journal of Physics: Condensed Matter* **26**, 103202 (2014).
- [41] García-Palacios, J. L. & Lázaro, F. J. Langevin-dynamics study of the dynamical properties of small magnetic particles. *Physical Review B* **58**, 14937 (1998).
- [42] d’Aquino, M., Serpico, C. & Miano, G. Geometrical integration of landau–lifshitz–gilbert equation based on the mid-point rule. *Journal of Computational Physics* **209**, 730–753 (2005).
- [43] Kittel, C. *Introduction to Solid State Physics* (Wiley, 2004). URL <https://books.google.nl/books?id=kym4QgAACAAJ>.
- [44] Bocdanov, A. & Hubert, A. The properties of isolated magnetic vortices. *physica status solidi (b)* **186**, 527–543 (1994).
- [45] Kézsmárki, I. *et al.* Néel-type skyrmion lattice with confined orientation in the polar magnetic semiconductor gav4s8. *Nature materials* **14**, 1116–1122 (2015).

- [46] Rogers, J. A., Maznev, A. A., Banet, M. J. & Nelson, K. A. Optical generation and characterization of acoustic waves in thin films: Fundamentals and applications. *Annual Review of Materials Science* **30**, 117–157 (2000).
- [47] Walt, S. v. d., Colbert, S. C. & Varoquaux, G. The numpy array: a structure for efficient numerical computation. *Computing in Science & Engineering* **13**, 22–30 (2011).
- [48] Press, W. H., Teukolsky, S. A., Vetterling, W. T. & Flannery, B. P. *Numerical recipes in C*, vol. 2 (Cambridge Univ Press, 1982).